A&A, 715, A356 (2026)
https://doi.org/10.1051/0004-6361/202662243
© The Authors 2026

Astronomy & Astrophysics

Euclid: Discovery of a quasar at $z = 8.13$ hosting a 360-million-solar-mass black hole★

J. Wolf, S. Belladitta, D. Yang, F. Guarneri, E. Bañados, J. F. Hennawi, J.-T. Schindler, R. E. Hviding, et al.

(Full author list and affiliations details can be found after the references)

Received 27 July 2026 / Accepted 8 October 2026

ABSTRACT

Quasars powered by rapid accretion onto supermassive black holes (SMBHs) have been uncovered deep into the first gigayear of cosmic history. Here we present the discovery of EUCL J150452.291+625224.39 (J1504+6252), selected from Euclid Wide Survey imaging and spectroscopically confirmed as the first quasar at $z > 8$ through a campaign with the Keck Observatory, the *Hubble* Space Telescope, the Large Binocular Telescope, and the *James Webb* Space Telescope (JWST). J1504+6252 exhibits the defining spectral signatures of archetypal quasars observed at a lower redshift, including a luminous blue power-law continuum and broad permitted emission lines, indicating the presence of a classical broad-line region. Using medium-resolution JWST/NIRSpec G395M spectroscopy, we determined a systemic redshift of $z_{\rm sys} = 8.129 \pm 0.005$, corresponding to only 630 Myr after the Big Bang and shifting the quasar redshift frontier by ≃39 Myr, or approximately 6% of the age of the Universe at that epoch. From the Hβ and Mg II emission lines, we measured intrinsic broad-line-region full widths at half maximum FWHM(Hβ,BLR) = 3160^{+270}_{-270} km s^{-1} and FWHM(Mg II,BLR) = 3740^{+160}_{-170} km s^{-1}, respectively. From a widely used single-epoch Hβ-based calibration, we measured a reference black hole mass of $\log_{10}(M_{\rm BH}/M_\odot) = 8.56^{+0.43}_{-0.43}$. Applying a range of single-epoch black hole mass calibrations to both Mg II and Hβ yields a broader interval of $\log_{10}(M_{\rm BH}/M_\odot) = 8.33$–$8.89$, with corresponding Eddington ratios of $\lambda_{\rm Edd} = 0.12$–0.44. Assembling a black hole of several hundred million solar masses within the first few hundred million years, despite its currently sub-Eddington accretion rate, requires either a massive seed or sustained, highly efficient early growth. The discovery of a mature, sub-Eddington quasar at $z > 8$ suggests that substantially more luminous quasars hosting similarly massive black holes may remain to be discovered. Conversely, the previously known re-ionisation-era quasars may represent the rapidly accreting end of a broader population of already massive black holes spanning a wider range of accretion states.

Key words. galaxies: high-redshift – quasars: general – quasars: supermassive black holes – quasars: individual: EUCL J150452.291+625224.39 – quasars: individual: J1504+6252 – quasars: individual: Dún Aonghasa

1. Introduction

Quasars are the most luminous persistent sources of radiation in the Universe (with absolute UV magnitudes of $M_{\rm UV} \lesssim -23$, e.g. Bañados 2026). The nuclear regions of quasars harbour actively accreting supermassive black holes (SMBHs), reaching 10^8–$10^{10}\,M_\odot$ (Fan et al. 2023, and references therein). Over the past three decades, the quasar redshift frontier has steadily advanced deep into the epoch of re-ionisation: from the first quasars beyond $z \approx 5$ (Fan et al. 1999, 2000; Stern et al. 2000), to $z \approx 6$ (Fan et al. 2001, 2003; Willott et al. 2007), to the first quasar beyond $z \approx 7$ (Mortlock et al. 2011), and, in rapid succession, three more at $z \approx 7.5$ (Bañados et al. 2018; Yang et al. 2020; Wang et al. 2021). Most recently, Yang et al. (2026) pushed the frontier to $z = 7.77$, corresponding to only about 660 Myr after the Big Bang, with the discovery of EUCL J172902.75+641018.1.

Together, these discoveries have extended our observational reach into the early Universe, in some cases by tens of millions of years. They have also opened several complementary channels for probing early cosmic history.

First, extending the quasar redshift frontier to earlier times places increasingly stringent constraints on black hole seeding and accretion models. The discovery of massive SMBHs at a progressively higher distance (e.g. Onoue et al. 2019; Yang et al. 2021; Farina et al. 2022; Bosman et al. 2025) leaves ever less time for their growth through conventional assembly pathways (Inayoshi et al. 2020).

Beyond constraining SMBH growth, as luminous background sources, the most distant quasars provide some of the longest sightlines through the intervening intergalactic medium (IGM), enabling studies of re-ionisation-era IGM opacity and metal enrichment (e.g. Davies et al. 2018a; Tie et al. 2024; Hennawi et al. 2025; Kist et al. 2026). Absorption features in their spectra, including damping-wing signatures and metal absorption systems (e.g. Rowlands et al. 2026), constrain the ionisation state, enrichment history, and large-scale opacity fluctuations of the IGM during the final stages of re-ionisation.

Quasars further mark rare, highly biased peaks in the underlying matter distribution and therefore trace the densest regions of the early large-scale structure (e.g. Eilers et al. 2024; Wang et al. 2026; Schindler et al. 2026; Huang et al. 2026). Their environments provide a unique view of the connection between the first rapidly growing SMBHs, massive galaxy overdensities, and the formation of protocluster-scale structure during the epoch of re-ionisation (e.g. Pizzati et al. 2024; Kapahtia et al. 2026).

Finally, on galactic scales, high-redshift quasars probe the early stages of SMBH–host coevolution (Kormendy & Ho 2013). Observations in the sub-millimitre regime reveal compact, $\lesssim$2 kpc dust-emitting regions, host dynamical masses of about 10^{10}–$10^{11}\,M_\odot$, and frequent companions (e.g. Decarli et al. 2017, 2018; Venemans et al. 2020; Neeleman et al. 2021; Belladitta et al. 2026), while imaging with the *James*

★ This paper is published on behalf of the Euclid Consortium.

Open Access article, published by EDP Sciences, under the terms of the Creative Commons Attribution License (https://creativecommons.org/licenses/by/4.0), which permits unrestricted use, distribution, and reproduction in any medium, provided the original work is properly cited.
This article is published in open access under the Subscribe to Open model. Open access funding provided by Max Planck Society.

Webb Space Telescope (JWST) Near-Infrared Camera (NIRCam, Rigby et al. 2023; Rieke et al. 2023) now enables direct stellar-mass measurements (e.g. Ding et al. 2023, 2025; Yue et al. 2024; Stone et al. 2024). These constraints suggest a mean $M_{\rm BH}$–$M_\star$ relation broadly consistent with later epochs but with about 1 dex scatter (Silverman et al. 2025), permitting highly overmassive SMBHs in modest-mass hosts (e.g. Stone et al. 2023; Yue et al. 2024).

Luminous quasars in the epoch of re-ionisation are exceptionally rare: at $z \simeq 7$, the cumulative co-moving space density is of the order of one source per Gpc^3 for quasars brighter than $M_{1450} \sim -25$, corresponding to a projected surface density of only one such quasar per about 130 deg^2, and it declines rapidly towards higher luminosities (e.g. Schindler et al. 2023; Matsuoka et al. 2023). To date, only seven quasars have been spectroscopically confirmed at $z > 7.5$ (Bañados et al. 2018; Yang et al. 2020; Wang et al. 2021; Yang et al. 2026). All were identified as optical dropouts in wide-area optical and near-infrared (NIR) imaging surveys: at these redshifts, neutral hydrogen absorption in the intervening IGM strongly suppresses flux bluewards of Ly α λ1216 (hereafter Ly α), producing a sharp optical-to-NIR colour break.

The *Euclid* mission (Euclid Collaboration: Mellier et al. 2025) started its wide survey in February 2024, following the launch of the spacecraft in July 2023. Using the first 1.5 yr of imaging survey data over approximately 3000 deg^2, Yang et al. (2026) spectroscopically confirmed 31 new quasars at $6.60 < z < 7.77$, increasing the number of known $z > 7.5$ quasars from three to seven. These objects were spectroscopically confirmed with ground-based observations on the Keck and Magellan telescopes.

The high cost of deep ground-based NIR spectroscopy and telluric absorption limit the accessible redshift and magnitude range. For instance, the faintest quasar Yang et al. (2026) were able to spectroscopically confirm is EUCL J101255.87+663058.0 with $J_{\rm E} = 23.0$ (see Sect. 2.1). Its confirmation required a 7800 s exposure with the Keck/Multi-Object Spectrograph for Infra-Red Exploration (MOSFIRE, McLean et al. 2010, 2012).

For these reasons, we have decided to pursue space-based follow-up programmes for faint *Euclid*-identified high-redshift quasar candidates. The *Hubble* Space Telescope (HST) Wide Field Camera 3 (WFC3; Kimble et al. 2008) GO 18112 programme[1] (PI: J. Wolf) and the JWST Near Infrared Spectrograph (NIRSpec; Jakobsen et al. 2022) GO 11173 programme[2] (PI: J.-T. Schindler) were designed to overcome the limits of ground-based observations.

Here we report the discovery of EUCL J150452.291+625224.39 (hereafter J1504+6252, nicknamed Dún Aonghasa), the first quasar confirmed at $z > 8$ and hence the most distant quasar currently known[3]. It was identified in the Euclid Wide Survey (EWS) and we describe the selection process in Sect. 2. In Sect. 3, we present its confirmation through NIR spectroscopic observations with Keck/MOSFIRE, HST/WFC3, the Large Binocular Telescope (LBT) Utility Camera in the Infrared (LUCI, Mandel et al. 2000; Seifert et al. 2003), and JWST/NIRSpec. In Sect. 4, we present the derivation of the nuclear properties from the JWST spectrum. In Sect. 5, we discuss this discovery in the context of early SMBH growth and the emergence of the first massive black holes. Finally, we present our conclusions in Sect. 6. Throughout this paper, we adopt the Planck 2018 cosmology from Planck Collaboration VI (2020) for all distance-dependent measurements, with $H_0 = 67.66\,{\rm km\,s^{-1}\,Mpc^{-1}}$, $\Omega_{\rm m} = 0.3111$, and $\Omega_\Lambda = 0.6889$, and use magnitudes with an AB zero-point (Oke & Gunn 1983). Unless stated otherwise, quoted values correspond to the posterior median, with uncertainties given by the 16th and 84th percentiles, representing equal-tailed 68% credible intervals.

2. Candidate selection

J1504+6252 was identified as a high-probability high-z quasar candidate in EWS imaging using a combination of advanced selection techniques and redshift estimate. Here we detail the identification and photometric redshift determination of the source from custom *Euclid* catalogues.

2.1. Deep imaging from the EWS

The EWS will cover about 14 000 deg^2 of the extragalactic sky over the nominal six-year mission (Euclid Collaboration: Mellier et al. 2025). Imaging is obtained with the Visible Camera (VIS, Euclid Collaboration: Cropper et al. 2025), providing a single broad optical band, $I_{\rm E}$, over 550–900 nm, and with the Near Infrared Spectrometer and Photometer (NISP, Euclid Collaboration: Jahnke et al. 2025), which provides NIR imaging in three bands (Euclid Collaboration: Schirmer et al. 2022): $Y_{\rm E}$ (949.6–1212.3 nm), $J_{\rm E}$ (1167.6–1567.0 nm), and $H_{\rm E}$ (1521.5–2021.4 nm). The nominal EWS depths are $I_{\rm E} \simeq 26.2$ and $Y_{\rm E}$, $J_{\rm E}$, $H_{\rm E} \simeq 24$–24.5, quoted as 5σ point-source limits.

2.2. Candidate selection

We built a custom candidate catalogue from *Euclid* VIS and NISP imaging. The detailed catalogue construction process is presented by Yang et al. (2026). Here, we only summarise the most important steps. First, we selected isolated, point-like NIR sources detected at signal-to-noise ratio (S/N) > 5 in either $J_{\rm E}$ or $H_{\rm E}$, and then applied an optical-dropout criterion using VIS photometry. Force point-spread-function (PSF) photometry was measured on either the native VIS/NISP stacks or, when available, the co-added MER mosaics, which assemble calibrated exposures into co-aligned, background-subtracted images on a common pixel grid (Euclid Collaboration: Romelli et al. 2026). The final dropout sample was defined by the colour criterion $I_{\rm E} - J_{\rm E} > 3.05$ using the newly measured PSF photometry before passing candidates to the quasar-selection pipelines.

To improve completeness and candidate reliability, the dropout catalogues were submitted to three independent quasar selection algorithms. The methodologies and method-specific success metrics are detailed in Yang et al. (2026); the three methods are:

[1] https://www.stsci.edu/hst-program-info/program/?program=18112

[2] https://www.stsci.edu/jwst/science-execution/program-information?id=11173

[3] We name this source Dún Aonghasa (Irish pronunciation: /duːn ˈeːŋgəsə/), after the prehistoric cliff-top fort on Inis Mór. Built at the Atlantic edge of Ireland, where land gives way to a vast oceanic horizon to the west, Dún Aonghasa evokes both a boundary and an invitation: an apparent end at the edge of the cliff, with much still hidden beyond it. Likewise, J1504+6252 stands at the current observational frontier of quasars, illuminating the threshold to even earlier times still waiting to be explored.

– Extreme Deconvolution High-Redshift Quasar selection (XDHZQSO, Nanni et al. 2022; Yang et al. 2024, 2026) modelling the quasar and contaminant populations in flux-ratio space, accounting for photometric uncertainties and their dependence on magnitude.
– An XGBoost classifier (Chen & Guestrin 2016) trained on simulated high-redshift quasars (Guarneri et al. 2026) and empirical contaminants to assign each source a quasar probability.
– Template-based spectral energy distribution (SED) fitting with `LePhare` (v2.2 Arnouts & Ilbert 2011), comparing quasar, galaxy, and stellar-contaminant solutions (Wolf et al. 2024).

Each method returned a numeric selection success metric and a photometric redshift estimate. The candidates that passed empirical thresholds were visually inspected to remove data artefacts or obvious astrophysical contaminants and were merged into a prioritised target list for spectroscopic follow-up.

J1504+6252 was selected by all three methods as a high-priority candidate. It was identified within the 3644 deg^2 observed region of the survey available in August 2025 and has measured PSF photometry $Y_E = 24.10 \pm 0.16$, $J_E = 22.96 \pm 0.06$, and $H_E = 22.67 \pm 0.06$ (see Table 2), with no significant detection in the optical I_E band down to the nominal (5σ) point-source depth of $I_E \simeq 26.2$ mag. The source is not covered by ancillary z-band imaging. The photometric redshift estimates from XDHZQSO, XGBoost, and SED fitting are respectively $z_{phot} \in \{8.20, 8.21, 7.98\}$. Combining the three estimates gives a mean photometric redshift of $\bar{z}_{phot} = 8.13 \pm 0.10$. This value informed the grism assignment for spectroscopic follow-up (see Sect. 3.2). *Euclid* cutouts of the source, together with a 30″-wide view of its surrounding field[4], are shown in Fig. 1. The object appears as an isolated red point source, with no evidence for multiple images, arcs, or an obvious deflector; the nearest foreground galaxy lies at a projected separation of ∼5″. Strong gravitational lensing is therefore unlikely, although modest, unresolved magnification cannot be excluded based on the available *Euclid* imaging.

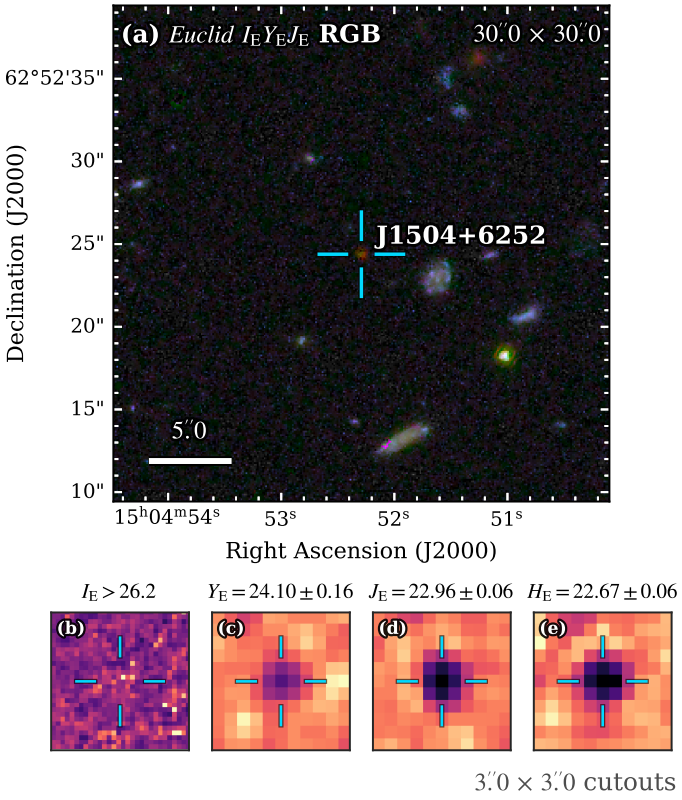


Fig. 1. *Euclid* imaging of J1504+6252. Panel (a) shows a 30″ × 30″ *Euclid* RGB image using I_E-, Y_E-, and J_E-band MER cutouts centred on the quasar, whose position is indicated by the cyan crosshairs. Panels (b)–(e) show 3″ × 3″ cutouts of the VIS and NISP stacks in the I_E, Y_E, J_E, and H_E bands, respectively, with cyan crosshairs marking the source position. J1504+6252 is undetected in the broad optical I_E band, is suppressed in Y_E, and is clearly detected in J_E and H_E, producing the sharp spectral break expected for a quasar at $z > 8$.

3. Quasar confirmation

The photometric redshift, $\bar{z}_{phot} \simeq 8.1$, and faintness of J1504+6252 motivated a tiered spectroscopic campaign combining deep ground- and space-based observations, each providing progressively stronger evidence for its quasar nature and redshift. An initial Keck/MOSFIRE long-slit spectrum revealed a blue continuum (Sect. 3.1), while HST/WFC3 provided tentative evidence for a spectral break (Sect. 3.2). This break and a flat continuum were subsequently established with a deep LBT/LUCI exposure (Sect. 3.3), and a final JWST/NIRSpec observation secured the redshift and delivered a high-quality, broad-wavelength-coverage spectrum for further analysis (Sect. 3.4). The spectroscopic campaign is summarised in Table 1. We did not use the *Euclid*/NISP slitless spectroscopic channel because, at $J_E \simeq 23$, the source is well below the expected continuum-detection limit of the EWS (Euclid Collaboration: Gillard et al. 2026).

Table 1. Summary of the spectroscopic observations of J1504+6252.

Telescope	Instrument	Grating/grism and filter	Date	t_{exp} [s]
Keck I	MOSFIRE	J2	2026-01-18	4800
HST	WFC3/IR	G141/F125W	2026-05-12	2206
LBT	LUCI1+LUCI2	G200/HKspec	2026-05-15	21 360
LBT	LUCI1+LUCI2	G200/zJspec	2026-05-16	23 520
JWST	NIRSpec	G140H/F100LP	2026-06-26	788
JWST	NIRSpec	G235H/F170LP	2026-06-26	591
JWST	NIRSpec	G395M/F290LP	2026-06-26	788

Notes. The listed exposure times are total on-source integration times. For the LBT observations, they refer to the retained exposures combined from LUCI1 and LUCI2. The WFC3/F125W image was obtained for source positioning and wavelength calibration of the G141 slitless spectrum.

3.1. Keck/MOSFIRE longslit spectroscopy

Initial spectroscopic follow-up was obtained with Keck/MOSFIRE on 2026-01-18 (U262, PI: J. Hennawi). The observations were carried out in longslit mode with the J2 filter, covering $\lambda_{obs} \simeq 1120$–$1250$ nm. We employed an ABAB dithering pattern for sky subtraction, with a total on-source exposure time of 4800 s. The MOSFIRE data were reduced with

[4] The composite image was produced with `eummy` (Schirmer 2026), which combines the *Euclid* imaging channels to preserve the VIS spatial resolution while optimally encoding the multi-band colour information.

PypeIt (Prochaska et al. 2020a,b, version 1.17.3) following the same procedure described in Yang et al. (2026).

The MOSFIRE spectrum shows a blue continuum detection down to the blue edge of the J2 bandpass (50% transmission at 1117 nm), consistent with a high-z quasar with the observed J_E magnitude. However, a spectral break was not covered within the observed range, constraining the redshift to $z \lesssim 8.2$. While these data could not, by themselves, localise the break, they established J1504+6252 as a promising $z \gtrsim 8$ quasar candidate, consistent with the photometric redshift.

3.2. HST/WFC3 slitless spectroscopy

HST GO 18112 (PI: J. Wolf) is a WFC3/IR slitless-spectroscopy snapshot programme designed to obtain spectra of *Euclid* high-redshift quasar candidates within a single HST orbit. The programme uses the WFC3/IR grisms G102 and G141, which cover 800–1150 nm and 1075–1700 nm, respectively. For each target, the grism setup is selected from the candidate photometric redshift: candidates with $z_{\rm phot,mean} - s_{\rm phot} < 8.0$ are observed with F105W pre-imaging and the G102 grism, while candidates with $z_{\rm phot,mean} - s_{\rm phot} > 8.0$ are observed with F125W pre-imaging and the G141 grism, to capture the Ly α-break[5].

J1504+6252 was observed as part of this programme on 2026-05-12, at the angle between the U3 axis of the telescope relative to north ORIENT(U3) = 177°, using the WFC3/IR G141 grism. The visit consisted of a direct F125W image with an exposure time of 113 s, followed by two dithered G141 spectroscopic exposures of 1103 s each, for a total grism exposure time of 2206 s.

The slitless spectroscopic data were reduced with Grizli (Brammer 2023, see for instance Watson et al. 2025 for the detail of the grism reduction). We began with the standard calibrated HST exposures and applied additional preprocessing to improve the quality of the direct and grism images, including astrometric alignment, masking of bad pixels and cosmic rays, and construction of combined direct-image mosaics used for source detection. The grism exposures were corrected for the spatially structured NIR background using scaled master-background models, with residual large-scale structure removed after masking object flux. Object catalogues and segmentation maps derived from the direct F125W image were then used to predict the position, trace, and wavelength solution of each dispersed spectrum. Grizli was used to model the full two-dimensional grism scene, including contamination from neighbouring sources, and to subtract this contamination before extracting individual spectra. The final products consist of contamination-corrected two-dimensional spectra and optimally extracted one-dimensional spectra, which were used for subsequent redshift and emission-line measurements.

The resulting 2D and 1D spectra are presented in Fig. 2. The HST/WFC3 G141 spectrum reveals a clear continuum detection redwards of a sharp break at $\lambda_{\rm obs} \simeq 1120$ nm, as expected from a Ly α absorption break at $z \simeq 8.1$. We fit the WFC3/G141 low-resolution spectrum with quasar templates following the approach of Bañados et al. (2023), Belladitta et al. (2025), and Martínez-Ramírez et al. (2026), and obtain a best-fit redshift of $z = 8.09$ with $\chi^2 = 45.6$ (53 degrees of freedom). The G141 grism resolution, $R \simeq 130$, corresponds to $\Delta\lambda \simeq 8$–10 nm at this wavelength, or $\Delta z \simeq 0.07$ for Ly α; allowing for the proximity of the break to the blue sensitivity limit and the uncertain break morphology, we quote a grism-based estimate of $z_{\rm grism} \simeq 8.1 \pm 0.1$. In addition, the spectrum shows a broad emission feature near $\lambda_{\rm obs} \simeq 1430$ nm, consistent with C IV λ1549 (hereafter C IV) at the same redshift. The combined presence of the Ly α break and broad high-ionisation emission identifies J1504+6252 as a quasar at $z \simeq 8.1$, confirming the *Euclid*-based photometric redshift. However, because the Ly α break lies close to the blue sensitivity limit of the G141 grism, additional spectroscopic follow-up was required to confirm the break and refine the redshift.

3.3. LBT/LUCI longslit spectroscopy

To independently confirm the spectral break seen near the blue edge of the HST/WFC3 G141 grism, and to extend the wavelength coverage, we obtained deep NIR long-slit spectroscopy of J1504+6252 with LBT/LUCI. The observations were carried out in binocular mode on 2026-05-15 and 2026-05-16 (programme ID: MPIA-2026A-001, PI E. Bañados). The observational setup on May 15 (16) used the G200 grating coupled with the HKspec (zJspec) filter on both the LUCI1 and LUCI2 arms. LUCI G200 with the zJ filter covers 900–1200 nm (with a central wavelength of 1170 nm), while the HK filter covers 1500–2400 nm (centred at 1930 nm). The zJspec setup is therefore expected to cover the Ly α break, while the HKspec setup is expected to detect the C III] λ1909 emission line. We employed the 1″ slit at a position angle of 280.°83 and utilised an ABBA dithering pattern for optimal sky subtraction. Individual science exposures were 240 s in both setups. Each setup consisted of 51 science exposures per LUCI arm, corresponding to 12 240 s per arm. However, due to poor seeing conditions during the two observing nights (with seeing degrading to 1.″8), not all exposures were used in producing the final spectrum shown in Fig. 2. For the zJspec setup, 49 exposures per arm were retained, yielding 98 individual exposures combining LUCI1 and LUCI2, for a total exposure time of 23 520 s. For the HKspec setup, 40 exposures from LUCI2 and 49 exposures from LUCI1 were retained, yielding a total of 89 exposures and a total exposure time of 21 360 s.

The LUCI spectra were reduced with PypeIt (version 1.16.1) using standard NIR long-slit reduction procedures (following e.g. Onorato et al. 2025; Belladitta et al. 2025). These include bias subtraction, flat fielding, sky subtraction, wavelength calibration using exposures of arc lamps, flux calibration using exposures of spectrophotometric standard stars, and telluric correction. The individual exposures were reduced separately, then combined with the coadd2d routine, and optimal extraction was applied to obtain the 1D spectrum. The final spectrum was flux calibrated to match the *Euclid* NIR photometry.

The resulting 2D and 1D LUCI spectra shown in Fig. 2 independently confirm the presence of the spectral break at $\lambda_{\rm obs} \simeq 1120$ nm inferred from the HST/WFC3 data, with continuum emission detected redwards of the break. From the scaled LBT/LUCI zJ and HK spectroscopy, we measure a rest-frame UV continuum spectral index of $\alpha_\lambda = -1.28$ ($f_\lambda \propto \lambda^{\alpha_\lambda}$). This relatively flat continuum is broadly consistent with typical quasar SEDs ($\alpha_\lambda \simeq -1.5$, e.g. Vanden Berk et al. 2001).

3.4. JWST/NIRSpec fixed slit spectroscopy

We subsequently performed follow-up restframe UV to optical spectroscopy of J1504+6252 with JWST. The observations were conducted on 2026-06-26 with NIRSpec in fixed-slit mode

[5] Here $z_{\rm phot,mean}$ denotes the mean photometric redshift from the three selection methods. $s_{\rm phot}$ is the standard deviation and is a measure of the dispersion among the methods. This quantity is only used for grism selection; it is not a formal photometric-redshift uncertainty.

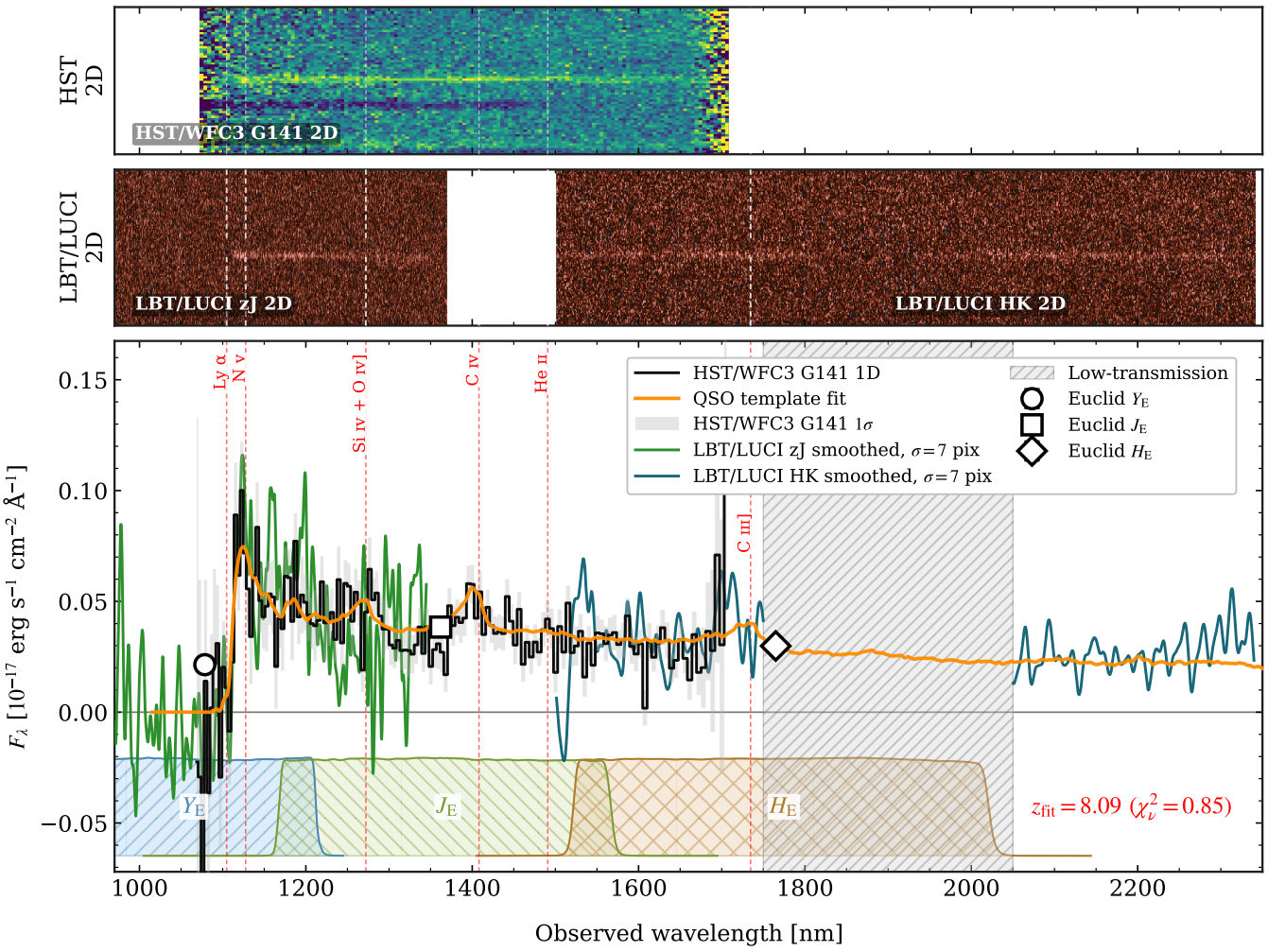


Fig. 2. Combined spectroscopic confirmation of J1504+6252. The upper panels show the two-dimensional spectra from HST/WFC3 G141 and LBT/LUCI G200 zJspec and HKspec. The lower panel compares the extracted HST/WFC3 G141 spectrum with the ground-based LUCI spectra and the best-fitting quasar template, with the spectra placed on a common flux scale using the *Euclid* Y_E, J_E, and H_E photometry. The *Euclid* photometric measurements are shown as open symbols, and the shaded bands indicate the corresponding *Euclid*/NISP filter transmission curves (Euclid Collaboration: Schirmer et al. 2022). The sharp continuum break at $\lambda_{obs} \simeq 1.1\,\mu m$ is identified as the Ly α break, yielding a template redshift of $z_{fit} = 8.09$ with $\chi^2_\nu = 0.86$. Grey shading shows the 1σ uncertainty on the HST/WFC3 spectrum. Vertical dashed lines mark the expected observed wavelengths of prominent rest-frame UV emission lines at the best-fitting redshift.

through the Director's Discretionary Discovery programme GO 12761[6] (PI: J. Wolf).

The target was observed in fixed-slit mode using the G140H/F100LP and G235H/F170LP high-resolution (R = 2700) configurations, as well as the G395M/F290LP medium-resolution (R = 1000) configuration. Target acquisition was performed with the F140X filter using the NRSRAPID readout pattern. The G140H and G235H observations used the S200A1/S200A2 fixed-slit configuration, the full detector subarray, the NRSIRS2RAPID readout pattern, one integration, and 56 and 42 groups, respectively. The G395M observation used the S200A2 fixed slit with the full detector subarray, NRSIRS2RAPID readout, one integration, and 56 groups. The total on-source integration times in the G140H/F100LP, G235H/F170LP, and G395M/F290LP gratings were 788 s, 591 s, and 788 s, respectively. Together, the three grating settings provide continuous coverage from the Ly α break through C IV, C III] λ1909, Mg II λ2800 (hereafter Mg II), Hβ, the [O III] $\lambda\lambda$4959,5007 doublet (hereafter [O III]) and the rest-frame UV/optical continuum, enabling a precise systemic redshift estimate and measurements of the quasar continuum and broad emission-line properties.

The fixed-slit exposures were processed from the uncalibrated data products using the JWST Calibration Pipeline (v1.20.2) with CRDS context map `jwst_1464.pmap`. Stages 1 and 2 (`calwebb_detector1` and `calwebb_spec2`) applied the standard detector-level corrections, assigned the wavelength solution, and performed the flat-field, point-source path-loss, and flux calibration steps using the CRDS reference files. We independently verified the absolute spectrophotometric calibration by computing synthetic Euclid measurements from the flux-calibrated NIRSpec spectrum. We obtain Y_E = 24.00, J_E = 22.94, and H_E = 22.70 mag, in good agreement with the measured Euclid photometry of Y_E = 24.10 ± 0.16, J_E = 22.96 ± 0.06, and H_E = 22.67 ± 0.06 mag. The synthetic photometry agrees with the Euclid measurements to within 0.1 mag in all three bands, corresponding to ∼10% in Y_E and better than 3% in J_E and H_E. We disabled the background subtraction, `resample_spec`, and `extract_1d` steps, and instead passed the

[6] https://www.stsci.edu/jwst/science-execution/program-information?id=12761

calibrated two-dimensional spectral images to `PypeIt` (v1.17.3). Sky subtraction was performed using `PypeIt`'s local sky-subtraction procedure, which jointly models the source profile and sky spectrum in each exposure. One-dimensional spectra were then optimally extracted for each exposure and grating setting. The individual spectra were placed on a common wavelength grid, scaled to a consistent flux level, and coadded with `PypeIt` to produce the final NIRSpec spectrum used for the redshift and emission-line analysis.

The combined spectrum from the three NIRSpec gratings is presented in Fig. 3. It unambiguously confirms the quasar nature of J1504+6252, showing a sharp Ly α break together with broad rest-frame UV and optical emission lines, including N V λ1240, C IV, C III] λ1909, Mg II, Hβ. These features firmly establish J1504+6252 as a quasar. In Appendix A, we present lower-redshift spectral analogues of J1504+6252 identified from Sloan Digital Sky Survey (SDSS) Data Release 14 (DR14) spectroscopy using a nearest-neighbour search in spectral space.

The spectrum also displays several distinctive features, including weak or undetected narrow [O III] emission. This characteristic, recently observed in both luminous $z > 7.5$ quasars and JWST AGN (e.g. Wolf et al. 2026; Caputi et al. 2026; Maiolino et al. 2026), may reflect a combination of low metallicity and collisional de-excitation at high gas densities in the nuclear region, although the absence of a clearly detected auroral [O III] λ4363 line challenges the high-density scenario (e.g. Maiolino et al. 2026; Ivey et al. 2026). A luminosity-dependent suppression may also contribute through the narrow-line Baldwin effect observed in Type 1 AGN, whereby the strength of [O III] relative to the AGN continuum decreases towards higher luminosities (Netzer et al. 2004; Stern & Laor 2012).

The spectrum also reveals a strongly blueshifted and asymmetric broad C IV emission-line profile (e.g. Meyer et al. 2019; Schindler et al. 2020). We estimate a velocity offset of $\sim$3500 km s^{-1} for the centroid of the broad component, indicative of nuclear outflows. A detailed analysis of the outflow and broad-line region properties will be presented in a forthcoming publication (Guarneri et al., in prep.). Finally, the quasar appears to be affected by a proximate damped Ly α system (e.g. Russell et al. 2006; Prochaska et al. 2008; Hennawi et al. 2009; Ellison et al. 2010), as indicated by the strongly damped Ly α profile and the associated metal absorption features (in particular Mg II) near the systemic redshift (e.g. Rowlands et al. 2026). These absorption features will be investigated in detail in a separate publication (Yang et al., in prep.). In the following section, we analyse the Hβ–[O III] and Mg II regions to determine the definitive systemic spectroscopic redshift and measure the accretion properties from the broad emission lines.

4. Results

4.1. Systemic redshift and black hole mass

We model the Hβ–[O III] region of the JWST/NIRSpec G395M spectrum with `unite` (Unified liNe Integration Turbo Engine), a Bayesian emission-line fitting framework[7] (Hviding 2026). `unite` forward-models the observed spectrum by combining continuum emission, line profiles, and the wavelength-dependent instrumental resolution, and samples the posterior distribution of the model parameters with a Hamiltonian Monte Carlo approach. The fit is performed over the observed-frame wavelength range 4000–4800 nm.

The spectral model comprises a power-law continuum, the optical Fe II template of Park et al. (2022), the Hβ emission complex, and the [O III] doublet. The Fe II template amplitude and intrinsic velocity width are fitted independently, with a uniform prior of 1000–15 000 km s^{-1} on its FWHM (e.g. Hu et al. 2008). To determine the level of complexity required by the Hβ profile, we compare three nested models: a single broad component; a narrow core; plus a broad component, and a narrow core plus intermediate- and broad-width components. We adopt uniform intrinsic FWHM priors of 30–700 km s^{-1}, 700–2500 km s^{-1}, and 2500–15 000 km s^{-1} for the narrow, intermediate, and broad components, respectively. The narrow Hβ component and the [O III] doublet are tied to a common redshift and velocity width, whereas the intermediate and broad Hβ components are allowed independent velocity offsets and widths. The [O III] doublet ratio is fixed to its atomic value, $F_{5007}/F_{4959} = 2.98$, and its flux is constrained to be non-negative so that, in the absence of a significant detection, the posterior yields a one-sided upper limit.

The preferred Hβ decomposition is selected using posterior-predictive model comparison where available, with the Bayesian information criterion used as a fallback. In either case, we retain the simplest model whose performance is statistically indistinguishable from that of the best-fitting alternative, and require any additional component to have a constrained, non-zero flux posterior. The model also includes a multiplicative scaling parameter for the NIRSpec/G395M line-spread function. All reported line widths are intrinsic because the model profiles are forward-convolved with the instrumental line-spread function (de Graaff et al. 2024) before comparison with the data. We present the result of this fit in Fig. 4. The detailed emission line properties of the decomposition are listed in Appendix B. The model comparison strongly favours the three-component Hβ decomposition, comprising narrow, intermediate, and broad components, with ΔBIC = 28.8 relative to the two-component model.

The [O III] doublet is not formally detected in the fit. We therefore quote a posterior 3σ upper limit of $L_{[\mathrm{O\,III}]\,\lambda5007} < 5.7 \times 10^{41}$ erg s^{-1}. We measure the relative strength of Fe II as $R_{\mathrm{FeII}} = F_{\mathrm{FeII}}(4434\text{–}4684\,\text{Å})/F_{\mathrm{H}\beta,\mathrm{BLR}}$, where the H$\beta$ BLR flux includes the intermediate and broad components, and obtain $R_{\mathrm{FeII}} = 0.77^{+0.06}_{-0.05}$. The independently fitted optical Fe II template requires an additional Gaussian convolution with a FWHM of 1270^{+190}_{-150} km s^{-1}[8].

We also note that we do not detect the host-galaxy [O II] λ3727 emission line, which could, in principle, provide an upper limit on the unobscured star-formation rate of the host galaxy (e.g. Feng et al. 2026); however, a quantitative assessment is beyond the scope of this discovery paper.

Because the [O III] doublet is not significantly detected, we determine the systemic redshift of J1504+6252 from the fitted narrow Hβ component (e.g. Bon et al. 2020). The [O III] doublet would generally be preferred as a systemic-redshift tracer because it arises in the narrow-line region and is less affected by broad-line-region kinematics, although its centroid can itself be shifted by ionised-gas outflows. Other available tracers, such as Mg II, are broad emission lines and therefore provide less precise constraints on the systemic velocity. The only significantly detected narrow lines in the G395M spectrum are Hβ and Hγ,

[7] https://github.com/TheSkyentist/unite/

[8] Because the empirical template already contains finite intrinsic line broadening, this quantity represents only the additional Gaussian convolution applied to the template and not the intrinsic width of the Fe II emission.

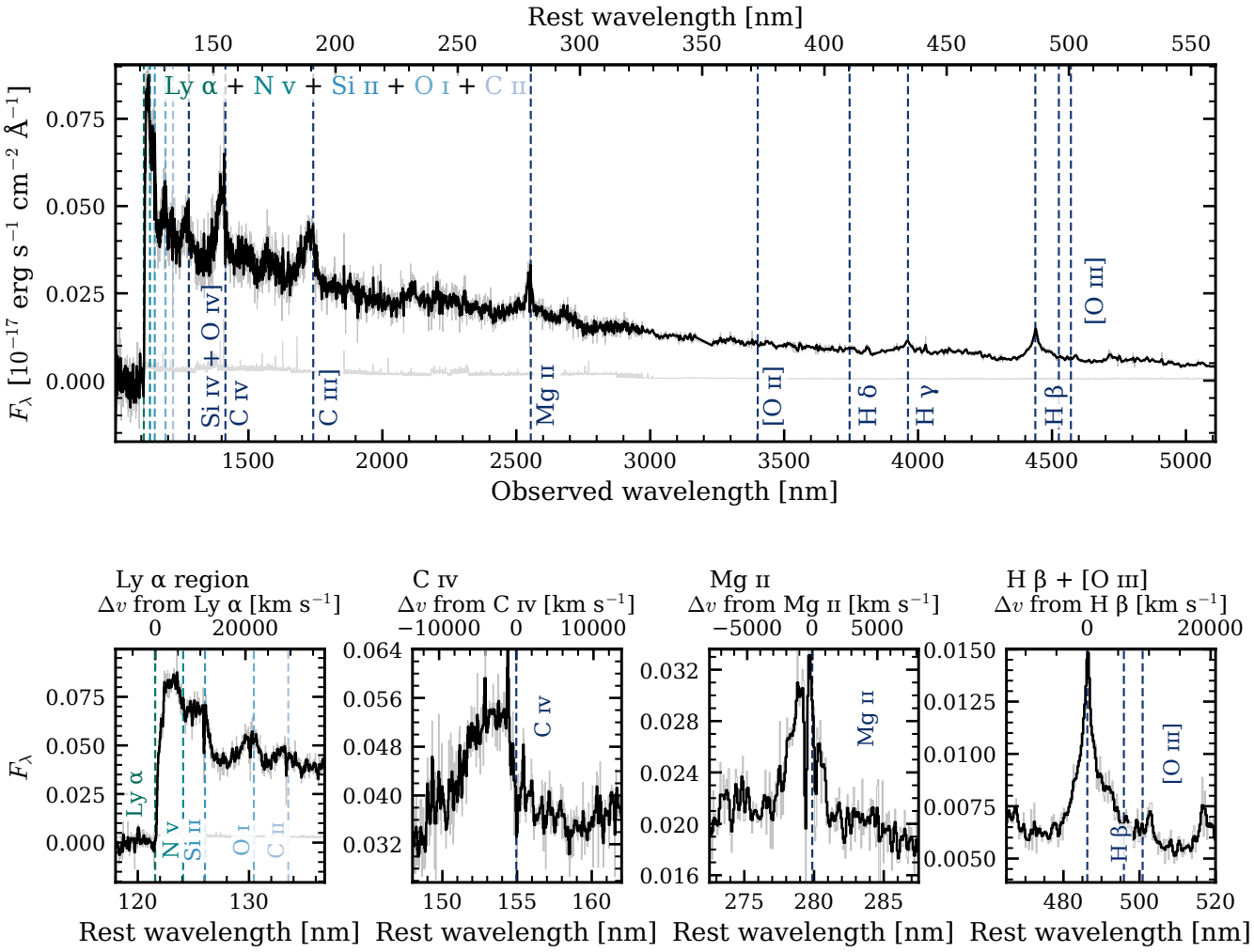


Fig. 3. JWST/NIRSpec spectrum of J1504+6252. The upper panel shows the combined fixed-slit NIRSpec spectrum in the observed frame, stitched together from the G140H, G235H, and G395M gratings, with the rest-frame wavelength axis shown at the top for the adopted redshift $z = 8.129$ (see Sect. 4). The black line shows the extracted one-dimensional spectrum and the grey curve shows the corresponding flux uncertainty. Vertical dashed lines mark the expected wavelengths of prominent rest-frame UV and optical emission lines. The lower panels show zoom-ins on the Ly α+N V λ1240, C IV, Mg II, and Hβ+[O III] regions. The NIRSpec spectrum reveals a sharp Ly α break, broad UV emission lines, and broad rest-frame optical Hβ emission, confirming J1504+6252 as a luminous broad-line quasar at $z > 8$. Additionally, an Mg II metal absorption feature is clearly detected close to the systemic redshift. The Ly α line profile shows substantial damping. The centroid of the broad C IV emission line is shifted by about ~3500 km s^{-1}, suggesting the presence of strong nuclear outflows.

and narrow Hβ therefore provides the best available rest-frame optical systemic-redshift indicator. Large-sample SDSS studies show that narrow Balmer lines generally remain close to the host-galaxy stellar velocity, supporting their use as systemic-redshift tracers when stellar absorption features are unavailable (Bae & Woo 2014).

We measure $z_{\rm sys,nar} = 8.129 \pm 0.005_{\rm tot}$ (where the total uncertainty accounts for $\pm 0.001_{\rm stat}$ statistical uncertainty and $\pm 0.005_{\rm sys}$ systematic uncertainty). The statistical and systematic components correspond to velocity uncertainties of approximately 33 and 150 km s^{-1}, respectively, with the total uncertainty dominated by the systematic term. The statistical uncertainty reflects the formal uncertainty on the fitted narrow-Hβ centroid. Although Bon et al. (2020) found that the narrow components of Hβ and [O III] were consistent with the mean stellar velocity to within 60 km s^{-1} in lower-redshift quasars, Bian et al. (2005) measured an object-to-object dispersion of 158 km s^{-1} between the narrow-Hβ and [O III] centroids in SDSS narrow-line Seyfert 1 galaxies, including a tail of strongly blueshifted [O III] sources. We therefore conservatively adopt a systematic uncertainty of 150 km s^{-1} to account for narrow-line-region kinematics and for the uncertain applicability of low-redshift calibrations to a luminous quasar at $z > 8$.

The intrinsic FWHM of the narrow component is 430^{+150}_{-110} km s^{-1}. The intermediate and broad Hβ components have intrinsic FWHMs of 2290^{+140}_{-220} km s^{-1} and 7800^{+530}_{-560} km s^{-1}, respectively. For the virial analysis, we define the broad-line-region profile as the sum of the intermediate and broad components, excluding the narrow core, and measure a FWHM of 3160^{+270}_{-270} km s^{-1}.

We convert the measured Hβ line width into black hole mass estimates using several calibrations that combine a luminosity-based proxy for the broad-line-region radius (Kaspi et al. 2000; Bentz et al. 2013), with the broad-line velocity width hereafter referred to as single-epoch calibrations (e.g. Greene & Ho 2005; Vestergaard & Peterson 2006; Shen et al. 2011). As our benchmark, we adopt the widely used continuum-based prescription of Vestergaard & Peterson (2006), facilitating direct comparison

with previous studies of luminous high-redshift quasars (e.g. Liu et al. 2024; Loiacono et al. 2024):

$$\log_{10}\left(\frac{M_{\rm BH}}{M_\odot}\right) = 6.91 + 0.50\log_{10}\left[\frac{\lambda L_\lambda(5100\,\text{Å})}{10^{44}\,\text{erg s}^{-1}}\right] + 2\log_{10}\left[\frac{\text{FWHM(H}\beta,\text{BLR})}{10^3\,\text{km s}^{-1}}\right]. \quad (1)$$

Here, $\lambda L_\lambda(5100\,\text{Å})$ is the featureless continuum luminosity at rest-frame 5100 Å (see Sect. 4.2), excluding the Fe II contribution. Applying the relation to the posterior samples of the continuum luminosity and total BLR profile, and including the intrinsic scatter of the calibration and the adopted object-to-object virial-factor uncertainty, we obtain

$$\log_{10}\left(\frac{M_{\rm BH}}{M_\odot}\right) = 8.56^{+0.07}_{-0.08}\,(\text{stat})^{+0.43}_{-0.43}\,(\text{tot}), \quad (2)$$

where the first quoted asymmetric uncertainty is statistical and the second one is the total uncertainty including systematics. We complement this benchmark estimate with two alternative Hβ prescriptions. The recent FWHM-based fundamental-plane calibration of Woo et al. (2026), applied to the same total BLR profile, yields $\log_{10}(M_{\rm BH}/M_\odot) = 8.33^{+0.38}_{-0.38}$. The broad H$\beta$ luminosity calibration of Dalla Bontà et al. (2020) instead gives $\log_{10}(M_{\rm BH}/M_\odot) = 8.89^{+0.40}_{-0.40}$. Our H$\beta$-based mass estimates rely on complementary calibrations: Vestergaard & Peterson (2006) use the optical continuum luminosity, whereas Dalla Bontà et al. (2020) use the broad Hβ luminosity as a proxy for the BLR radius, thereby reducing sensitivity to host-galaxy contamination. Finally, Woo et al. (2026) include the Eddington ratio as an additional parameter in their calibration, accounting empirically for accretion-rate-dependent departures from the standard radius–luminosity relation.

As an independent consistency check, we also estimate the black hole mass from the Mg II doublet covered by the G235H grating. With our `unite` framework, we fit the Mg II region over the observed-frame wavelength range 2300–2900 nm, masking absorption features that overlap the emission-line profile and would otherwise bias its inferred shape and width. In this spectral window, we use the Fe II template of Salviander et al. (2007), who reconstruct the emission beneath Mg II from the Vestergaard & Wilkes (2001) template using the theoretical Fe II model of Sigut & Pradhan (2003). As for the Hβ region, we compare models containing one, two, and three kinematic components and select the simplest adequate model. The single broad-component model is preferred, with an intrinsic FWHM of 3740^{+160}_{-170} km s^{-1}.

We first apply the established Mg II calibration of Vestergaard & Osmer (2009), obtaining $\log_{10}(M_{\rm BH}/M_\odot) = 8.76^{+0.55}_{-0.55}$. For comparison, the Mg II fundamental-plane calibration of Woo et al. (2026) yields $\log_{10}(M_{\rm BH}/M_\odot) = 8.50^{+0.39}_{-0.39}$. The fit to the Mg II region is shown in the lower panel of Fig. 4.

All Hβ- and Mg II-based estimates are mutually consistent within their uncertainties and are summarised in Table 2. We quote the Vestergaard & Peterson (2006) Hβ result as our benchmark single-epoch mass estimate, while recognising that the dominant uncertainty arises from the adopted calibration. The extreme central values span

$$\log_{10}\left(\frac{M_{\rm BH}}{M_\odot}\right) = 8.33\text{–}8.89, \quad (3)$$

which we use to represent the calibration-dependent range of plausible black hole masses for J1504+6252.

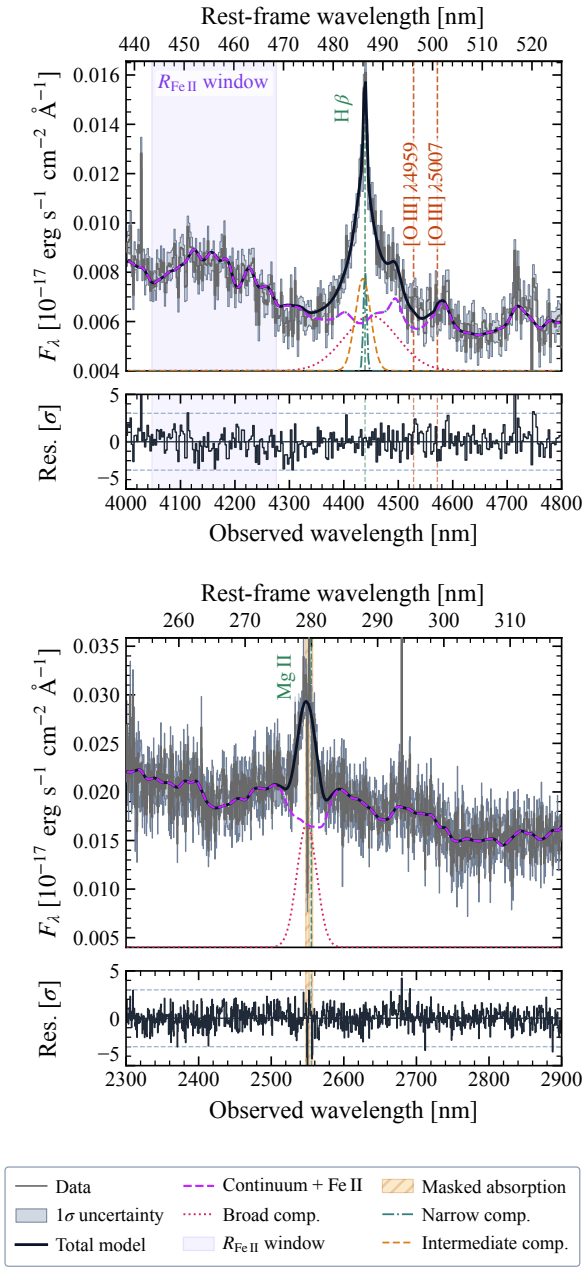


Fig. 4. Fit to the Hβ–[O III] (top) and Mg II (bottom) regions of J1504+6252. For each region, the upper panel shows the JWST/NIRSpec spectral fit. The observed spectrum is shown as the dark grey histogram, and the 1σ flux uncertainty is indicated in light grey. The best-fitting total model is shown as the solid black curve, while the continuum is shown as the dashed magenta curve. Individual emission-line model components are shown as coloured offset curves. In the Hβ panel, the shaded purple region marks the rest-frame wavelength interval used to measure $R_{\rm FeII}$ from the Fe II template component. In the Mg II panel, the hatched orange region marks the automatically masked narrow absorption region excluded from the fit. Vertical dashed lines mark the expected observed wavelengths of systemic narrow Hβ, [O III], and Mg II. No significant [O III] emission is detected. The lower panels show the residuals in units of the flux uncertainty. The horizontal lines in the residual panel delimit the 3σ range.

4.2. Continuum luminosity and Eddington rate

We measure the UV magnitude at 145 nm, M_{1450}, from a sigma-clipped, inverse-variance-weighted linear continuum fit over

142.5–147.5 nm in the rest frame, corresponding to the G235H portion of the JWST/NIRSpec spectrum. For all luminosity measurements, we include a 5% systematic uncertainty to account for the absolute flux calibration accuracy of the NIRSpec fixed-slit spectroscopy quoted by the JWST documentation at the time of writing[9]. We obtain $F_\lambda(145\,\mathrm{nm}) = (3.47 \pm 0.18) \times 10^{-19}\,\mathrm{erg\,s^{-1}\,cm^{-2}\,\AA^{-1}}$, corresponding to $M_{1450} = -24.08 \pm 0.06$. We then measure the monochromatic continuum luminosity at rest-frame 510 nm from the best-fitting Hβ–[O III] spectral model, obtaining $\log_{10}\left[\lambda L_\lambda(5100\,\mathrm{\AA})/(\mathrm{erg\,s^{-1}})\right] = 45.30 \pm 0.02$.

We convert the monochromatic quantity to a bolometric luminosity using the luminosity-dependent correction of Runnoe et al. (2012b), accounting for the correction presented by Runnoe et al. (2012a). Here, L_{iso} is the isotropic-equivalent bolometric luminosity inferred from the observed continuum:

$$\log_{10}\left[\frac{L_{\mathrm{iso}}}{\mathrm{erg\,s^{-1}}}\right] = 4.891 + 0.912\,\log_{10}\left[\frac{\lambda L_\lambda(5100\,\mathrm{\AA})}{\mathrm{erg\,s^{-1}}}\right]. \quad (4)$$

We then adopt $L_{\mathrm{bol}} = 0.75\,L_{\mathrm{iso}}$, which results in

$$\log_{10}\left[\frac{L_{\mathrm{bol}}}{\mathrm{erg\,s^{-1}}}\right] = 46.08 \pm 0.02. \quad (5)$$

Combining this bolometric luminosity with the black hole mass estimates presented in Sect. 4, we compute the Eddington ratio as $\lambda_{\mathrm{Edd}} = L_{\mathrm{bol}}/L_{\mathrm{Edd}}$, where $L_{\mathrm{Edd}} = 1.26 \times 10^{38}\,(M_{\mathrm{BH}}/M_\odot)\,\mathrm{erg\,s^{-1}}$ (e.g. Netzer 2013). Across the adopted Hβ and Mg II single-epoch calibrations, we obtain central values spanning

$$\lambda_{\mathrm{Edd}} = 0.12\text{–}0.44. \quad (6)$$

with the individual measurements and uncertainties listed in Table 2. Thus, J1504+6252 is inferred to be accreting at approximately 12–44% of the Eddington limit, depending on the adopted black hole mass calibration. These values place it towards the lower envelope of the $z > 6$ quasar population, although such values are not unprecedented, as shown in Fig. 5.

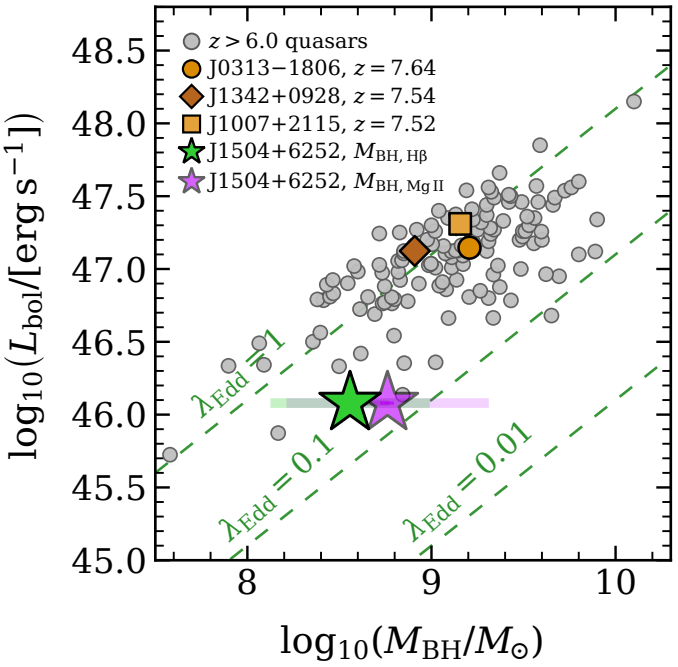


Fig. 5. L_{bol} versus M_{BH} for quasars $z > 6.0$ from the literature (Belladitta et al. 2025, and references therein) and J1504+6252. Brown symbols mark the previously most distant quasars with black hole mass measurements (Bañados et al. 2018; Yang et al. 2020; Wang et al. 2021). The two stars show the Hβ and Mg II based M_{BH} measurements for J1504+6252, using the calibrations from Vestergaard & Peterson (2006) and Vestergaard & Osmer (2009), respectively. Dashed lines indicate constant Eddington ratios. J1504+6252 is offset in terms of its Eddington rate with respect to the bulk of the known $z > 6$ quasar population.

5. A new quasar redshift frontier: Implications for SMBH growth

In Fig. 6, we compare J1504+6252 to the known high-redshift quasar population (Fan et al. 2023, and references therein) in the M_{1450}–redshift plane, together with spectroscopically confirmed galaxies (Smit & Bowler 2026, and references therein) and JWST-selected lower-luminosity AGN (Larson et al. 2023; Kokorev et al. 2023; Harikane et al. 2023; Maiolino et al. 2024a,b; Napolitano et al. 2025; Juodžbalis et al. 2026), including Little Red Dots and the more recently defined Little Blue Dots (LRDs and LBDs; Hviding et al. 2025; de Graaff et al. 2026; Taylor et al. 2025; Tanaka et al. 2025; Geris et al. 2026). J1504+6252 extends the confirmed quasar redshift frontier beyond $z = 8$. Its luminosity places it above the bulk of the known galaxy and LRD populations at similar redshifts, but within the extrapolation of the luminous quasar sequence to earlier times. The broad rest-frame UV and optical emission lines, high UV luminosity, and large black hole mass of J1504+6252 identify it as a luminous, unobscured quasar powered by a mature accreting SMBH.

While evidence for massive black hole growth at higher redshift has been reported previously, those systems probe a fundamentally different population. The physical nature of LRDs, for instance, remains under active debate, with several observed systems pointing towards accreting black holes embedded in extremely dense gas environments (e.g. Ji et al. 2025; de Graaff et al. 2025; Naidu et al. 2026), a picture also explored in theoretical models involving compact, optically thick gaseous envelopes and super-Eddington accretion (e.g. Inayoshi & Maiolino 2025; Kido et al. 2025), while alternative interpretations invoke no actively accreting black hole at all (Baggen et al. 2024). The JWST identification of compact sources with blue SEDs that have been termed LBDs has raised the possibility that these objects and LRDs may represent related manifestations of a common underlying population. In proposed unified scenarios, differences in circumnuclear obscuration, its geometry, and/or viewing orientation can produce the observed diversity in SED shape (Brazzini et al. 2026; Madau & Maiolino 2026). JWST has also uncovered evidence for SMBH accretion in several galaxies at $z > 8.5$ through broad emission lines (e.g. CEERS_1019, Larson et al. 2023, although Zamora et al. 2025 find evidence for outflow-driven line broadening), high-density gas tracers and typical AGN emission lines (GN-z11, Maiolino et al. 2024b), and emission-line diagnostics combined with X-ray observations (GHZ9, Kovács et al. 2024; Napolitano et al. 2025). UHZ1, at $z = 10.073$, has been interpreted as a heavily obscured AGN associated with a lensed galaxy based on reported X-ray emission (Bogdán et al. 2024; Goulding et al. 2023), although its AGN nature remains

[9] https://jwst-docs.stsci.edu/jwst-calibration-status/nirspec-calibration-status/

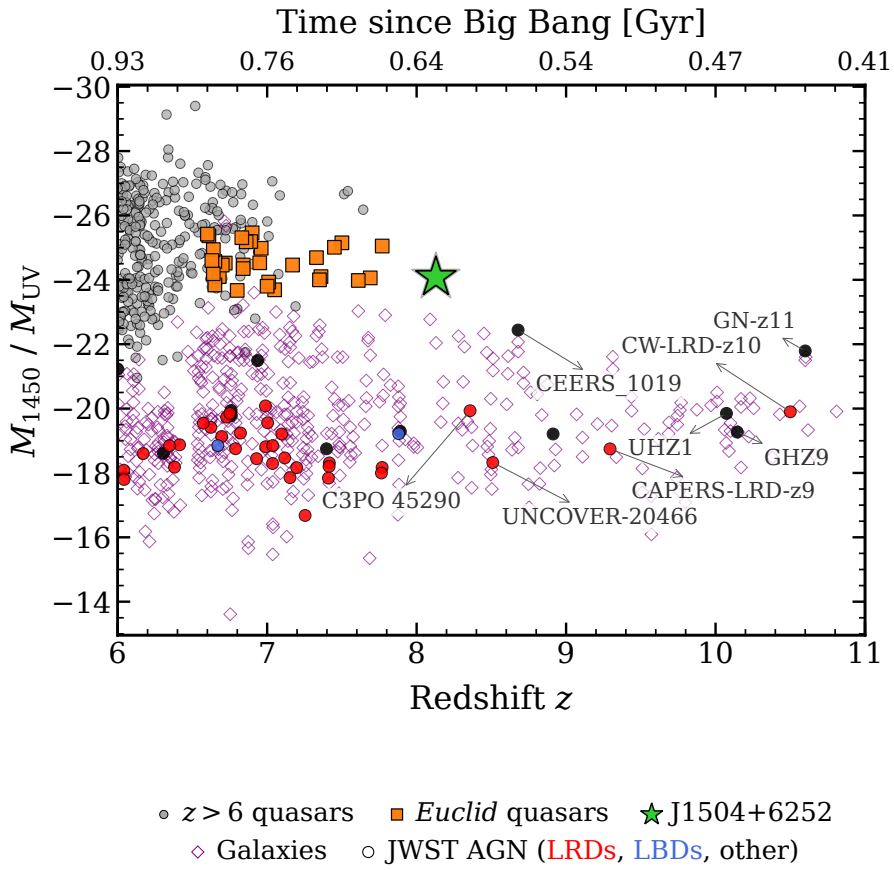


Fig. 6. Absolute UV magnitude, M_{1450} or M_{UV}, as a function of redshift for high-redshift quasars, galaxies, LRDs, LBDs, and other JWST-selected AGN up to $z = 11$. Previously known quasars are shown as grey circles (Fan et al. 2023, and references therein, as well as quasars discovered by Yang et al. 2023, Wolf et al. 2024, Belladitta et al. 2025, and Martínez-Ramírez et al. 2026). Orange squares show recently identified *Euclid* quasars from Yang et al. (2026). Lyman-break galaxies are shown as open purple diamonds; see Harikane et al. (2025), Smit & Bowler (2026), and references therein. JWST-selected AGN are shown as circles and colour-coded according to their phenomenological classification: LRDs in red, LBDs in blue, and other AGN in black. The latter include sources from Larson et al. (2023), Kokorev et al. (2023), Harikane et al. (2023), Maiolino et al. (2024a), Maiolino et al. (2024b), Napolitano et al. (2025), and Juodžbalis et al. (2026). The LRD sample is drawn from de Graaff et al. (2026), Tanaka et al. (2025, including the spectroscopic confirmation of CW-LRD-z10 at $z > 10$ from T. Tanaka, pers. comm.), and Geris et al. (2026), while LBDs are taken from Geris et al. (2026). The green star marks J1504+6252, which is more UV-luminous than the LRDs, other JWST-selected AGN, and Lyman-break galaxies at comparable redshifts.

debated (Álvarez-Márquez et al. 2026; Zou et al. 2026). In contrast, J1504+6252 is the first spectroscopically confirmed luminous quasar at $z > 8$ and exhibits the canonical spectral characteristics of lower-redshift quasars, as highlighted by the SDSS nearest neighbour search in Appendix A. In particular, its luminosity and broad emission lines enable the robust application of single-epoch black hole mass estimators calibrated using analogous quasar samples at lower redshift. J1504+6252 directly reveals an accreting SMBH with a mass of $\sim 10^{8.5}\,M_\odot$ accreting at ∼26% of the Eddington limit. Its discovery demonstrates that by $z = 8.129$, only about 630 million years after the Big Bang, at least some SMBHs had already completed their obscured growth phase and evolved into the luminous quasar population.

The existence of J1504+6252 at $z = 8.13$ places new constraints on the early growth of black holes. With a black hole mass of $\log_{10}(M_{BH}/M_\odot) = 8.3$–$8.9$ at this cosmic epoch, the source leaves limited time for growth from low-mass seeds. In particular, remnant seeds from Population III stars with $M_{seed} \sim 10^2\,M_\odot$, often invoked at $z \sim 20$ (e.g. Volonteri 2010; Inayoshi et al. 2020), if limited by Eddington accretion, require extremely rapid and nearly uninterrupted growth to reach the observed mass by this epoch while more massive seed channels can substantially relax the growth requirement (e.g. Natarajan 2011). Heavy seeds from the direct collapse of pristine gas clouds, emerging around $z \simeq 15$–20 (e.g. Trinca et al. 2026), were therefore introduced to alleviate the black hole growth timescale problem (e.g. Bromm & Loeb 2003; Lodato & Natarajan 2006, 2007; Volonteri et al. 2008; Habouzit et al. 2016). Alternatively, runaway collisions in dense nuclear star clusters have been presented as a possible formation channel for intermediate-mass black holes (e.g. Devecchi & Volonteri 2009; Katz et al. 2015; Sakurai et al. 2017). Primordial black holes (PBHs) provide another possible pathway (Carr & Hawking 1974; Rubin et al. 2001; Carr & Silk 2018), because sufficiently massive PBHs formed in the early Universe can seed dark matter halo assembly and subsequently grow through gas accretion (e.g. Dayal 2024; Ziparo et al. 2025; Dayal 2026).

Beyond accretion, black-hole mergers may contribute to SMBH assembly. Recent JWST studies, however, indicate major-galaxy-merger rates of ≃2–6 events per galaxy per Gyr at $z \gtrsim 6$ (e.g. Duan et al. 2025; Calabrò et al. 2026). Integrated over the ∼0.45 Gyr between $z \sim 20$ and $z = 8.13$, such rates correspond to an expected ≃1–3 major galaxy mergers along the main progenitor branch. The number of completed black-hole coalescences is likely smaller, because both progenitors must host black holes and because dynamical friction, binary hardening, and gravitational-wave inspiral introduce additional delays (e.g. Volonteri et al. 2020). Because mergers have an additive effect on black-hole mass, they are thus unlikely by themselves to assemble a $10^{8.3}$–$10^{8.9}\,M_\odot$ black hole by $z = 8.13$ unless the progenitors were already massive. Consistently, Pacucci & Loeb (2020) predict that accretion generally dominates the growth of $M_{BH} > 10^8\,M_\odot$ black holes at $z > 6$.

Figure 7 illustrates the new constraints imposed by the discovery of J1504+6252 using backtraced growth histories anchored to the measured mass of the quasar. As a physically motivated starting point for the growth histories, we adopt $z_{seed} = 20$, representative of the earliest epochs commonly invoked for the formation of massive seeds. PBHs constitute an exception, as they may form much earlier in the early Universe. For radiatively

Table 2. Summary of the observed and derived properties of J1504+6252.

Property	Value	
Source properties		
ID	EUCL J150452.291+625224.39	
Name	Dún Aonghasa	
RA (J2000)	15:04:52.291	
Dec (J2000)	+62:52:24.39	
$z_{\rm sys,nar}$	$8.129 \pm 0.001_{\rm stat} \pm 0.005_{\rm sys}$	
M_{1450} [AB mag]	-24.08 ± 0.06	
Euclid Photometry		
Band	*AB* magnitude	f_ν [μJy]
$I_{\rm E}$	>26.2	-0.009 ± 0.009
$Y_{\rm E}$	24.10 ± 0.16	0.833 ± 0.124
$J_{\rm E}$	22.96 ± 0.06	2.385 ± 0.136
$H_{\rm E}$	22.67 ± 0.06	3.109 ± 0.169
Emission-line and continuum properties		
FWHM(Hβ,BLR)	3160^{+270}_{-270} km s^{-1}	
FWHM(Mg II,BLR)	3740^{+160}_{-170} km s^{-1}	
$R_{\rm FeII}$	$0.77^{+0.06}_{-0.05}$	
$\log_{10} L_{\rm H\beta,BLR}$	$43.52^{+0.03}_{-0.03}$ erg s^{-1}	
$\log_{10} \lambda L_\lambda(3000\,\text{Å})$	$45.51^{+0.02}_{-0.02}$ erg s^{-1}	
$\log_{10} \lambda L_\lambda(5100\,\text{Å})$	$45.30^{+0.02}_{-0.02}$ erg s^{-1}	
$\log_{10} L_{\rm bol}$	$46.08^{+0.02}_{-0.02}$ erg s^{-1}	
Single-epoch cal.	$\log_{10}(M_{\rm BH}/M_\odot)$	$\lambda_{\rm Edd}$
Hβ-based		
W26	$8.33^{+0.10\,(+0.38)}_{-0.11\,(-0.38)}$	$0.44^{+0.12\,(+0.62)}_{-0.09\,(-0.26)}$
DB20	$8.89^{+0.05\,(+0.40)}_{-0.06\,(-0.40)}$	$0.12^{+0.02\,(+0.19)}_{-0.01\,(-0.08)}$
VP06	$8.56^{+0.07\,(+0.43)}_{-0.08\,(-0.43)}$	$0.26^{+0.05\,(+0.45)}_{-0.04\,(-0.17)}$
Mg II-based		
W26	$8.50^{+0.05\,(+0.39)}_{-0.06\,(-0.39)}$	$0.30^{+0.04\,(+0.44)}_{-0.04\,(-0.18)}$
VO09	$8.76^{+0.04\,(+0.55)}_{-0.04\,(-0.55)}$	$0.17^{+0.02\,(+0.42)}_{-0.02\,(-0.12)}$

Notes. The coordinates correspond to the centroid of the *Euclid* NISP $J_{\rm E}$-band detection of J1504+6252, as determined by the *Euclid* NIR catalogue-extraction pipeline (Euclid Collaboration: Polenta et al. 2026). The *Euclid* photometry is based on PSF flux measurements. The systemic redshift is measured from the narrow Hβ component. The FWHM of the Hβ BLR component is measured from the sum of the intermediate and broad components. The FWHM of the Mg II BLR component is measured from the broad-line profile. The bolometric luminosity is computed from $\lambda L_\lambda(5100\,\text{Å})$ using the luminosity-dependent bolometric correction of Runnoe et al. (2012b), with the coefficients provided by Runnoe et al. (2012a). The quoted uncertainty on $L_{\rm bol}$ propagates only the uncertainty in $\lambda L_\lambda(5100\,\text{Å})$ through the fixed central bolometric correction. The uncertainties in the Runnoe et al. (2012b) coefficients are not included because the covariance between the fitted intercept and slope is unavailable. W26, DB20, VP06, and VO09 refer to Woo et al. (2026), Dalla Bontà et al. (2020), Vestergaard & Peterson (2006), and Vestergaard & Osmer (2009), respectively. For $M_{\rm BH}$ and $\lambda_{\rm Edd}$, the first uncertainty is statistical, while the value in parentheses is the total uncertainty including the intrinsic scatter and adopted systematic uncertainty of the corresponding single-epoch mass calibration. The total $\lambda_{\rm Edd}$ uncertainties do not include an additional uncertainty from the Runnoe et al. (2012b) bolometric-correction calibration.

efficient accretion, the growth curves are computed using the standard exponential black hole growth equation (Salpeter 1964, see also, e.g. Volonteri 2010),

$$\frac{{\rm d}M_{\rm BH}}{{\rm d}t} = \frac{1-\epsilon}{\epsilon}\frac{\lambda_{\rm Edd}}{t_{\rm Edd}} f_{\rm duty}\, M_{\rm BH}, \tag{7}$$

where ϵ is the radiative efficiency, $\lambda_{\rm Edd}$ is the Eddington ratio during active accretion, $f_{\rm duty}$ is the active accretion duty cycle, and $t_{\rm Edd} = 0.45$ Gyr. For constant ϵ, $\lambda_{\rm Edd}$, and $f_{\rm duty}$, the solution is

$$M_{\rm BH}(t) = M_{\rm seed} \exp\left[\frac{1-\epsilon}{\epsilon}\frac{\lambda_{\rm Edd} f_{\rm duty}}{t_{\rm Edd}}\,(t - t_{\rm seed})\right]. \tag{8}$$

The curves in Fig. 7 are obtained from this expression and are forced to pass through the observed black hole mass of J1504+6252 at $z = 8.13$, or through the measured black hole masses of the three previously most distant quasars at their observed redshifts (Bañados et al. 2018; Yang et al. 2020; Wang et al. 2021). We explore two families of illustrative black hole growth models. The first assumes radiatively efficient, Eddington-limited accretion, with $\lambda_{\rm Edd} = 1$ and a canonical radiative efficiency of $\epsilon = 0.10$. Our fiducial model further assumes continuous accretion, $f_{\rm duty} = 1$, and is shown for J1504+6252 and the comparison quasars. We then vary the duty cycle over $f_{\rm duty} = 0.3$–1.0, while keeping $\lambda_{\rm Edd} = 1$ and $\epsilon = 0.10$, to illustrate the effect of intermittent Eddington-limited growth.

The second family models super-critical accretion, for which the mass inflow rate exceeds the rate associated with the Eddington luminosity. We define

$$\dot{m} \equiv \frac{\dot{M}_{\rm inflow}}{\dot{M}_{\rm Edd}}, \qquad \dot{M}_{\rm Edd} \equiv \frac{L_{\rm Edd}}{\epsilon c^2}, \tag{9}$$

with $\epsilon = 0.10$ (e.g. King & Muldrew 2016). At high $\dot{m}$ ($\dot{m} \gg 1$), photon trapping, advection, and winds cause the converted luminosity to increase less rapidly than the mass inflow rate (Shakura & Sunyaev 1973; Abramowicz et al. 1988; Poutanen et al. 2007; Madau & Dickinson 2014). Following the classical super-critical-disc approximation of Shakura & Sunyaev (1973, see also, e.g. King & Muldrew 2016), we adopt

$$\lambda_{\rm Edd} \simeq 1 + \ln \dot{m}. \tag{10}$$

The corresponding effective radiative efficiency is $\epsilon_{\rm eff} = \epsilon\lambda_{\rm Edd}/\dot{m}$, decreasing from 0.10 to 0.070 over the adopted range $\dot{m} = 1$–3. Much lower efficiencies (as low as $\sim 10^{-3}$) have been integrated over the growth histories of $z > 7$ quasars (Davies et al. 2019). We show continuous-growth tracks with $f_{\rm duty} = 1$ and $\dot{m} = 1$–3. The $\dot{m} = 1$ case recovers the fiducial Eddington-limited model with $\lambda_{\rm Edd} = 1$ and $\epsilon_{\rm eff} = 0.10$, while larger $\dot{m}$ produces faster black hole growth with only a modest increase in emergent luminosity.

Within the radiatively efficient models at fixed ϵ, the inferred seed mass is highly sensitive to the duty cycle. Adopting $z_{\rm seed} = 20$, continuous Eddington-limited accretion with $\epsilon = 0.10$ requires a seed mass of $\sim 10^5\, M_\odot$, placing it towards the massive-seed regime and well above the characteristic masses expected for Pop III remnants. For this model, J1504+6252 provides constraints consistent with those inferred for previously discovered $z \sim 7.5$ quasars (Bañados et al. 2018; Yang et al. 2020; Wang et al. 2021). Progressively lower duty cycles require increasingly massive seeds, moving beyond the characteristic direct-collapse black-hole seed masses considered here. Within the strict assumptions of these toy models and adopting $z_{\rm seed} = 20$, duty cycles below approximately $f_{\rm duty} \simeq 0.5$ would require seed masses above the populations considered here in order to reproduce the observed mass of J1504+6252 by $z = 8.13$.

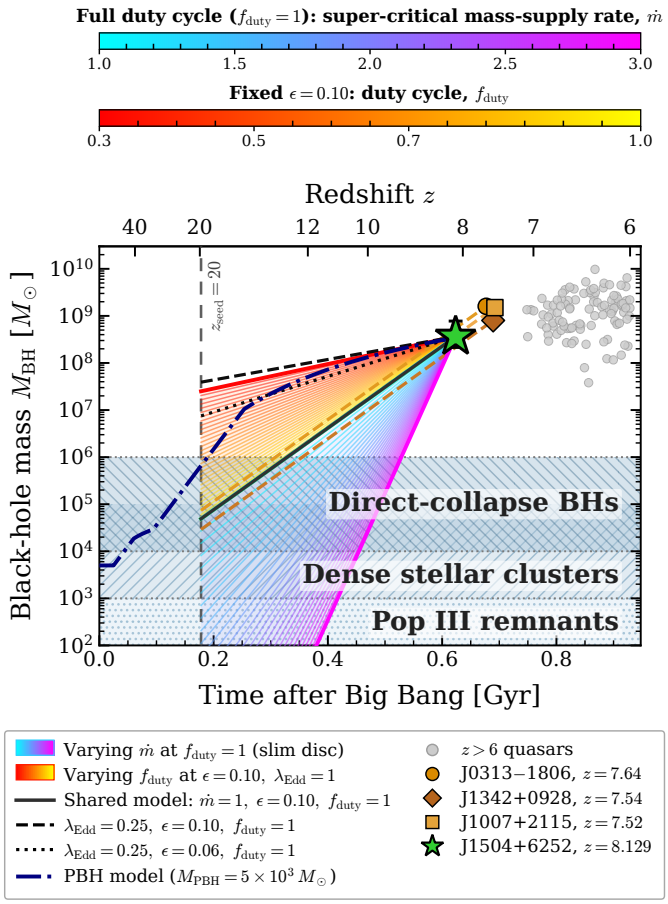


Fig. 7. Black hole growth curves for J1504+6252 (green star). Quasars at $z > 6$ with black hole mass measurements are shown in grey. Orange symbols mark the previously known highest-redshift quasars ($z \simeq 7.5$; Bañados et al. 2018; Yang et al. 2020; Wang et al. 2021), and the corresponding dashed curves show their growth histories assuming $\epsilon = 0.10$, $\lambda_{\rm Edd} = 1$, and $f_{\rm duty} = 1$ backtraced to $z_{\rm seed} = 20$. The coloured regions show two families of growth models anchored to the black hole mass estimate for J1504+6252 based on the calibration of Vestergaard & Peterson (2006). The error bar spans the central mass estimates obtained from all adopted Hβ and Mg II calibrations. The blue–violet models assume continuous super-critical accretion, with $f_{\rm duty} = 1$ and $\dot{m} = 1.0$–3.0, adopting $\lambda_{\rm Edd} \simeq 1 + \ln \dot{m}$ and the corresponding effective radiative efficiency. The red–yellow models instead assume radiatively efficient, Eddington-limited accretion with $\epsilon = 0.10$ and vary the duty cycle over $f_{\rm duty} = 0.3$–1.0. The solid black curve marks the common limiting model, corresponding to $\dot{m} = 1$, $\lambda_{\rm Edd} = 1$, $\epsilon = 0.10$, and $f_{\rm duty} = 1$. The dashed and dotted black curves show examples of sub Eddington growth with $\lambda_{\rm Edd} = 0.25$. The navy dot–dashed curve shows an illustrative primordial-black-hole-seeded assembly history, including halo growth and gas-supply-limited accretion, based on the model of Dayal (2024). Horizontal shaded regions indicate characteristic seed-mass ranges associated with Population III remnants, runaway stellar collisions in dense clusters, and direct-collapse black holes (Inayoshi et al. 2020).

This constraint can be substantially relaxed by enabling super-critical accretion. Because photon trapping reduces the effective radiative efficiency (e.g. Shimura & Manmoto 2003), a larger fraction of the supplied rest mass can fall into the black hole without a proportional increase in the emergent luminosity. The super-critical tracks therefore permit substantially lower seed masses, extending into the characteristic Population III remnant regime. Rapid mass assembly does not necessarily need to occur during archetypical Type 1 UV-luminous quasar phases. The comparison between the black hole mass density at $z \simeq 6$ and that inferred from the UV-luminous quasar population indicates that UV-luminous quasars may account for less than ten percent of the early black hole mass growth (Jahnke 2025). This may indicate that most of the growth occurs in obscured systems, radiatively inefficient phases, and potentially super-critical accretion episodes. An independent indication for buried growth comes from the discovery of a blazar at $z \sim 7$: the implied parent population of randomly aligned jets suggests that a substantial population of rapidly growing, potentially obscured SMBHs may remain undetected in UV-based quasar selections (Bañados et al. 2025).

Nevertheless, feedback from black hole accretion and supernovae can deplete or expel gas from the shallow gravitational potentials of low-mass seeds, thereby strongly suppressing mass assembly (e.g. Johnson & Bromm 2007; Whalen et al. 2008; Milosavljević et al. 2009; Alvarez et al. 2009; Inayoshi et al. 2020). Moreover, continued thin-disc accretion is expected to increase the spin of the black hole and thereby increase its radiative efficiency (Thorne 1974; Volonteri et al. 2005). The super-critical tracks should therefore only be interpreted as illustrating the growth rates required for light seeds to remain viable.

We also show a realisation of PBH-seeded growth based on the assembly model of Dayal (2024). The adopted realisation starts from a $5\times10^3\,M_\odot$ primordial black hole at matter–radiation equality, which acts as a seed, assembling a dark-matter halo around itself. The black hole remains effectively dormant until the halo becomes sufficiently massive to retain baryons, corresponding to a density of 200 times the critical density. For the black hole seed mass considered here, this corresponds to a redshift of $z \sim 75$. After this, gas can cool to form stars, and the black hole starts growing through gas accretion. Given its low mass, the black hole initially accretes close to the Eddington rate, albeit with fluctuations, down to $z \sim 15$. The Eddington fraction subsequently declines towards lower redshift, from $f_{\rm Edd} \sim 1$ at $z \gtrsim 20$ to ∼0.15 by $z \simeq 8$, as growth becomes increasingly supply-limited due to a combination of black hole and supernova feedback. The pronounced change in slope of the track reflects the evolving accretion rate. This scenario likewise provides a viable pathway for assembling a near-billion-solar-mass black hole within the first 630 million years of cosmic history.

J1504+6252 provides a new benchmark for models of early black hole growth by pushing the required assembly to still earlier times. However, the discovery of J1504+6252 does not enable a robust distinction between these formation pathways.

Strikingly, J1504+6252 has a comparatively low Eddington ratio relative to other known $z > 6$ quasars (Fig. 5). From the Hβ-based black hole mass and bolometric luminosity, we infer $\lambda_{\rm Edd} = 0.26^{+0.05}_{-0.04}$ from the calibration of Vestergaard & Peterson (2006) and a range $\lambda_{\rm Edd} = 0.12$–0.44 from all single-epoch calibrations. Thus, although the SMBH is already massive, it is not currently accreting close to the Eddington limit. The discovery of a sub-Eddington quasar with $\log_{10}(L_{\rm bol}/[{\rm erg\,s^{-1}}]) \sim 46$ at $z > 8$ therefore suggests that substantially brighter members of the same black hole population may remain to be discovered if they are not enshrouded in dust. At fixed black hole mass, increasing the accretion rate from the benchmark value $\lambda_{\rm Edd} \simeq 0.26$ to $\lambda_{\rm Edd} = 1$ would increase the luminosity by a factor of 3.8, corresponding to a brightening of 1.46 mag. An Eddington-limited analogue of J1504+6252 would thus have approximately $J_{\rm E} = 21.5$, $H_{\rm E} = 21.2$, and $M_{1450} = -25.5$, making it easily accessible to *Euclid*. If J1504+6252 is representative of the emerging $z > 8$ population, its low $\lambda_{\rm Edd}$ would imply that some billion-solar-mass black holes had already completed their most rapid growth phase by this

epoch. In either case, the presence of such a massive black hole in a comparatively low-accretion state requires efficient mass assembly at even earlier times, followed by a decline to the observed sub-Eddington phase.

6. Conclusions

We have presented the discovery of the quasar J1504+6252, a source we name Dún Aonghasa. Initially selected from *Euclid* imaging, J1504+6252 required a sequence of ground- and space-based NIR spectroscopic observations to confirm its nature as the most distant quasar known to date. From the narrow Hβ emission line, we measure a systemic redshift of $z = 8.129 \pm 0.005$, pushing the quasar redshift frontier about 39 Myr (or by 6%) earlier in cosmic history than the previous record holder at $z = 7.77$ (Yang et al. 2026). Based on the width of the broad Hβ emission line, we infer a benchmark single-epoch black hole mass of $\log_{10}(M_{\rm BH}/M_\odot) = 8.56^{+0.43}_{-0.43}$ using the Vestergaard & Peterson (2006) calibration, while the central values obtained from all adopted Hβ and Mg II calibrations span $\log_{10}(M_{\rm BH}/M_\odot) = 8.33$–$8.89$. The corresponding Eddington ratios span $\lambda_{\rm Edd} = 0.12$–0.44, indicating that the quasar is accreting at a comparatively low rate relative to much of the known $z > 6$ quasar population. Dún Aonghasa establishes a new quasar redshift frontier as the first confirmed quasar at $z > 8$, providing a powerful new benchmark for early SMBH growth.

The comparatively low instantaneous accretion rate of J1504+6252 extends the emerging picture of the earliest quasar population. Its large black hole mass shows that substantial growth must have occurred before the epoch at which the source is observed, whereas its current bolometric luminosity is not consistent with a phase of rapid mass assembly. The discovery of J1504+6252 implies that early massive black holes may occupy a broader range of accretion states than is represented by the predominantly luminous, rapidly accreting systems identified at $z > 6$ to date.

Euclid Collaboration: Barnett et al. (2019) predicted that *Euclid* should identify approximately 8–23 quasars at $z > 8$ over a survey area of ∼14 000 deg^2, with the range driven primarily by assumptions about the evolution of the quasar luminosity function at the highest redshifts. Scaling this prediction to the ∼3644 deg^2 considered here yields an expectation of ∼2–6 quasars. However, the extensive spectroscopic follow-up campaign required to discover J1504+6252 highlights the practical challenges of identifying such objects should there indeed be more to discover. As the survey area and follow-up coverage expand, *Euclid* will provide a clearer picture of the size of the $z > 8$ quasar population, and thereby provide unparalleled constraints on the abundance and growth of the earliest massive black holes.

Acknowledgements. We thank the anonymous referee for their constructive comments and suggestions, which have helped us improve the clarity and presentation of the paper. We thank Joseph Shields, Dave Thompson, and the staff of the Large Binocular Telescope (LBT) for their support of this work. The authors also gratefully acknowledge the assistance of our primary STScI support contacts, Patricia Royle and Alison Vick, as well as Amanda Pagul, Anton Koekemoer, and Cheryl Pavlovsky, whose support made the discovery observations possible. This research was supported by the Excellence Cluster ORIGINS, which is funded by the Deutsche Forschungsgemeinschaft (DFG, German Research Foundation) under Germany's Excellence Strategy – EXC 2094/2 – 390783311. RD acknowledges support from the INAF RF 2024 mini-grant "The interstellar medium at high redshift" and from the PRORIS 2025 "COSMOWEBB". MC acknowledges support from INAF RF 2024 GO grant "Revealing the nature of bright galaxies at cosmic dawn with deep JWST spectroscopy". The Euclid Consortium acknowledges the European Space Agency and a number of agencies and institutes that have supported the development of *Euclid*, in particular the Agenzia Spaziale Italiana, the Austrian Forschungsförderungsgesellschaft funded through BMIMI, the Belgian Science Policy, the Canadian Euclid Consortium, the Deutsches Zentrum für Luft- und Raumfahrt, the DTU Space and the Niels Bohr Institute in Denmark, the French Centre National d'Etudes Spatiales, the Fundação para a Ciência e a Tecnologia, the Hungarian Academy of Sciences, the Ministerio de Ciencia, Innovación y Universidades, the National Aeronautics and Space Administration, the National Astronomical Observatory of Japan, the Netherlandse Onderzoekschool Voor Astronomie, the Norwegian Space Agency, the Research Council of Finland, the Romanian Space Agency, the Swiss Space Office (SSO) at the State Secretariat for Education, Research, and Innovation (SERI), and the United Kingdom Space Agency. A complete and detailed list is available on the *Euclid* web site (www.euclid-ec.org/consortium/community/). Some of the data presented herein were obtained at Keck Observatory, which is a private 501(c)3 non-profit organisation operated as a scientific partnership among the California Institute of Technology, the University of California, and the National Aeronautics and Space Administration. The Observatory was made possible by the generous financial support of the W. M. Keck Foundation. The authors wish to recognise and acknowledge the very significant cultural role and reverence that the summit of Maunakea has always had within the Native Hawaiian community. We are most fortunate to have the opportunity to conduct observations from this mountain. This research is based on observations made with the NASA/ESA *Hubble* Space Telescope obtained from the Space Telescope Science Institute, which is operated by the Association of Universities for Research in Astronomy, Inc., under NASA contract NAS 5–26555. These observations are associated with programme18112 (PI: J. Wolf). This paper includes data from the LBT (programmeID: MPIA-2026A-001, PI E. Bañados). The LBT is an international collaboration among institutions in the United States and Europe. At the time data were acquired for this research, LBT Corporation Members were the University of Arizona on behalf of the Arizona Board of Regents; Istituto Nazionale di Astrofisica, Italy; and The Ohio State University, representing The Ohio State University, University of Notre Dame, University of Minnesota, and University of Virginia. This research used the facilities of the Italian Center for Astronomical Archives (IA2) operated by INAF at the Astronomical Observatory of Trieste. Observations have benefited from the use of ALTA Center (alta.arcetri.inaf.it) forecasts performed with the Astro-Meso-Nh model. Initialization data of the ALTA automatic forecast system come from the General Circulation Model (HRES) of the European Centre for Medium Range Weather Forecasts. This work is based in part on observations made with the NASA/ESA/CSA *James Webb* Space Telescope. The data were obtained from the *Mikulski* Archive for Space Telescopes at the Space Telescope Science Institute, which is operated by the Association of Universities for Research in Astronomy, Inc., under NASA contract NAS 5-03127 for JWST. These observations are associated with program #12761 (PI: J. Wolf). This research made use of `PypeIt` (https://pypeit.readthedocs.io/en/stable/) version 1.17.3, a Python package for semi-automated reduction of astronomical slit-based spectroscopy. Funding for the Sloan Digital Sky Survey V has been provided by the Alfred P. Sloan Foundation, the Heising-Simons Foundation, the National Science Foundation, and the Participating Institutions. SDSS acknowledges support and resources from the Center for High-Performance Computing at the University of Utah. SDSS telescopes are located at Apache Point Observatory, funded by the Astrophysical Research Consortium and operated by New Mexico State University, and at Las Campanas Observatory, operated by the Carnegie Institution for Science. The SDSS web site is www.sdss.org. SDSS is managed by the Astrophysical Research Consortium for the Participating Institutions of the SDSS Collaboration, including the Carnegie Institution for Science, Chilean National Time Allocation Committee (CNTAC) ratified researchers, Caltech, the Gotham Participation Group, Harvard University, Heidelberg University, The Flatiron Institute, The Johns Hopkins University, L'Ecole polytechnique fédérale de Lausanne (EPFL), Leibniz-Institut für Astrophysik Potsdam (AIP), Max-Planck-Institut für Astronomie (MPIA Heidelberg), Max-Planck-Institut für Extraterrestrische Physik (MPE), Nanjing University, National Astronomical Observatories of China (NAOC), New Mexico State University, The Ohio State University, Pennsylvania State University, Smithsonian Astrophysical Observatory, Space Telescope Science Institute (STScI), the Stellar Astrophysics Participation Group, Universidad Nacional Autónoma de México, University of Arizona, University of Colorado Boulder, University of Illinois at Urbana-Champaign, University of Toronto, University of Utah, University of Virginia, Yale University, and Yunnan University. This work made use of Astropy (https://www.astropy.org), a community-developed core Python package and an ecosystem of tools and resources for astronomy.

References

Abramowicz, M. A., Czerny, B., Lasota, J. P., & Szuszkiewicz, E. 1988, ApJ, 332, 646

Alvarez, M. A., Wise, J. H., & Abel, T. 2009, ApJ, 701, L133
Álvarez-Márquez, J., Colina, L., Crespo-Gomez, A., et al. 2026, A&A, submitted [arXiv:2602.02323]
Arnouts, S., & Ilbert, O. 2011, Astrophysics Source Code Library [record ascl:1108.009]
Bae, H.-J., & Woo, J.-H. 2014, ApJ, 795, 30
Baggen, J. F. W., van Dokkum, P., Brammer, G., et al. 2024, ApJ, 977, L13
Bañados, E. 2026, ArXiv e-prints [arXiv:2603.21976]
Bañados, E., Venemans, B. P., Mazzucchelli, C., et al. 2018, Nature, 553, 473
Bañados, E., Schindler, J.-T., Venemans, B. P., et al. 2023, ApJS, 265, 29
Bañados, E., Le Brun, V., Belladitta, S., et al. 2025, MNRAS, 542, 1088
Belladitta, S., Bañados, E., Xie, Z.-L., et al. 2025, A&A, 699, A335
Belladitta, S., Decarli, R., Bañados, E., et al. 2026, A&A, 711, A150
Bentz, M. C., Denney, K. D., Grier, C. J., et al. 2013, ApJ, 767, 149
Bian, W., Yuan, Q., & Zhao, Y. 2005, MNRAS, 364, 187
Bogdán, Á., Goulding, A. D., Natarajan, P., et al. 2024, Nat. Astron., 8, 126
Bon, N., Marziani, P., Bon, E., et al. 2020, A&A, 635, A151
Bosman, S. E. I., Ďurovčíková, D., Davies, F. B., & Eilers, A.-C. 2021, MNRAS, 503, 2077
Bosman, S. E. I., Álvarez-Márquez, J., Davies, F. B., et al. 2025, ApJ, submitted [arXiv:2511.02902]
Brammer, G. 2023, http://doi.org/10.5281/zenodo.8370018
Brazzini, M., D'Eugenio, F., Maiolino, R., et al. 2026, A&A, 713, A332
Bromm, V., & Loeb, A. 2003, ApJ, 596, 34
Calabrò, A., Pentericci, L., Llerena, M., et al. 2026, A&A, 714, A287
Caputi, K. I., Cooper, R. A., Rinaldi, P., et al. 2026, ApJ, 1007, 203
Carr, B. J., & Hawking, S. W. 1974, MNRAS, 168, 399
Carr, B., & Silk, J. 2018, MNRAS, 478, 3756
Carswell, R. F., Whelan, J. A. J., Smith, M. G., Boksenberg, A., & Tytler, D. 1982, MNRAS, 198, 91
Chen, T., & Guestrin, C. 2016, ArXiv e-prints [arXiv:1603.02754]
Dalla Bontà, E., Peterson, B. M., Bentz, M. C., et al. 2020, ApJ, 903, 112
Dall'Aglio, A., Wisotzki, L., & Worseck, G. 2008, A&A, 480, 359
Davies, F. B., Hennawi, J. F., Bañados, E., et al. 2018a, ApJ, 864, 142
Davies, F. B., Hennawi, J. F., Bañados, E., et al. 2018b, ApJ, 864, 143
Davies, F. B., Hennawi, J. F., & Eilers, A.-C. 2019, ApJ, 884, L19
Dayal, P. 2024, A&A, 690, A182
Dayal, P. 2026, OJA, submitted [arXiv:2604.20966]
de Graaff, A., Rix, H.-W., Carniani, S., et al. 2024, A&A, 684, A87
de Graaff, A., Rix, H.-W., Naidu, R. P., et al. 2025, A&A, 701, A168
de Graaff, A., Hviding, R. E., Naidu, R. P., et al. 2026, MNRAS, 551, stag1567
Decarli, R., Walter, F., Venemans, B. P., et al. 2017, Nature, 545, 457
Decarli, R., Walter, F., Venemans, B. P., et al. 2018, ApJ, 854, 97
Devecchi, B., & Volonteri, M. 2009, ApJ, 694, 302
Ding, X., Onoue, M., Silverman, J. D., et al. 2023, Nature, 621, 51
Ding, X., Onoue, M., Silverman, J. D., et al. 2025, ApJ, 993, 91
Duan, Q., Conselice, C. J., Li, Q., et al. 2025, MNRAS, 540, 774
Eilers, A.-C., Mackenzie, R., Pizzati, E., et al. 2024, ApJ, 974, 275
Ellison, S. L., Prochaska, J. X., Hennawi, J., et al. 2010, MNRAS, 406, 1435
Euclid Collaboration (Barnett, R., et al.) 2019, A&A, 631, A85
Euclid Collaboration (Schirmer, M., et al.) 2022, A&A, 662, A92
Euclid Collaboration (Cropper, M., et al.) 2025, A&A, 697, A2
Euclid Collaboration (Jahnke, K., et al.) 2025, A&A, 697, A3
Euclid Collaboration (Mellier, Y., et al.) 2025, A&A, 697, A1
Euclid Collaboration (Gillard, W., et al.) 2026, A&A, 707, A227
Euclid Collaboration (Polenta, G., et al.) 2026, A&A, 711, A3
Euclid Collaboration (Romelli, E., et al.) 2026, A&A, 711, A4
Fan, X., Strauss, M. A., Schneider, D. P., et al. 1999, AJ, 118, 1
Fan, X., White, R. L., Davis, M., et al. 2000, AJ, 120, 1167
Fan, X., Narayanan, V. K., Lupton, R. H., et al. 2001, AJ, 122, 2833
Fan, X., Strauss, M. A., Schneider, D. P., et al. 2003, AJ, 125, 1649
Fan, X., Bañados, E., & Simcoe, R. A. 2023, ARA&A, 61, 373
Farina, E. P., Schindler, J.-T., Walter, F., et al. 2022, ApJ, 941, 106
Feng, X., Wu, X.-B., Fu, Y., et al. 2026, Universe, 12, 214
Geris, S., Maiolino, R., Ji, X., et al. 2026, ArXiv e-prints [arXiv:2606.21614]
Goulding, A. D., Greene, J. E., Setton, D. J., et al. 2023, ApJ, 955, L24
Greene, J. E., & Ho, L. C. 2005, ApJ, 630, 122
Guarneri, F., Schindler, J. T., Meyer, R. A., et al. 2026, A&A, 709, A241
Habouzit, M., Volonteri, M., Latif, M., Dubois, Y., & Peirani, S. 2016, MNRAS, 463, 529
Harikane, Y., Zhang, Y., Nakajima, K., et al. 2023, ApJ, 959, 39
Harikane, Y., Inoue, A. K., Ellis, R. S., et al. 2025, ApJ, 980, 138
Hennawi, J. F., Prochaska, J. X., Kollmeier, J., & Zheng, Z. 2009, ApJ, 693, L49
Hennawi, J. F., Kist, T., Davies, F. B., & Tamanas, J. 2025, MNRAS, 539, 2621
Hu, C., Wang, J.-M., Ho, L. C., et al. 2008, ApJ, 687, 78
Huang, J., Hennawi, J., Pizzati, E., et al. 2026, MNRAS, submitted [arXiv:2602.04974]
Hviding, R. E. 2026, https://doi.org/10.5281/zenodo.20734477
Hviding, R. E., de Graaff, A., Miller, T. B., et al. 2025, A&A, 702, A57
Inayoshi, K., & Maiolino, R. 2025, ApJ, 980, L27
Inayoshi, K., Visbal, E., & Haiman, Z. 2020, ARA&A, 58, 27
Ivey, L. R., D'Eugenio, F., Maiolino, R., et al. 2026, MNRAS, stag1220
Jahnke, K. 2025, Open J. Astrophys., 8, 9
Jakobsen, P., Ferruit, P., Alves de Oliveira, C., et al. 2022, A&A, 661, A80
Ji, X., Maiolino, R., Übler, H., et al. 2025, MNRAS, 544, 3900
Johnson, J. L., & Bromm, V. 2007, MNRAS, 374, 1557
Juodžbalis, I., Maiolino, R., Baker, W. M., et al. 2026, MNRAS, 546, stag086
Kapahtia, A., Pillepich, A., Braspenning, J., et al. 2026, MNRAS, submitted [arXiv:2606.13784]
Kaspi, S., Smith, P. S., Netzer, H., et al. 2000, ApJ, 533, 631
Katz, H., Sijacki, D., & Haehnelt, M. G. 2015, MNRAS, 451, 2352
Kido, D., Ioka, K., Hotokezaka, K., Inayoshi, K., & Irwin, C. M. 2025, MNRAS, 544, 3407
Kimble, R. A., MacKenty, J. W., O'Connell, R. W., & Townsend, J. A. 2008, SPIE Conf. Ser., 7010, 70101E
King, A., & Muldrew, S. I. 2016, MNRAS, 455, 1211
Kist, T., Hennawi, J. F., Davies, F. B., et al. 2026, MNRAS, 545, staf2219
Kokorev, V., Fujimoto, S., Labbe, I., et al. 2023, ApJ, 957, L7
Kormendy, J., & Ho, L. C. 2013, ARA&A, 51, 511
Kovács, O. E., Bogdán, Á., Natarajan, P., et al. 2024, ApJ, 965, L21
Larson, R. L., Finkelstein, S. L., Kocevski, D. D., et al. 2023, ApJ, 953, L29
Liu, W., Fan, X., Yang, J., et al. 2024, ApJ, 976, 33
Lodato, G., & Natarajan, P. 2006, MNRAS, 371, 1813
Lodato, G., & Natarajan, P. 2007, MNRAS, 377, L64
Loiacono, F., Decarli, R., Mignoli, M., et al. 2024, A&A, 685, A121
Madau, P., & Dickinson, M. 2014, ARA&A, 52, 415
Madau, P., & Maiolino, R. 2026, A&A, 714, A276
Maiolino, R., Scholtz, J., Curtis-Lake, E., et al. 2024a, A&A, 691, A145
Maiolino, R., Scholtz, J., Witstok, J., et al. 2024b, Nature, 627, 59
Maiolino, R., Übler, H., D'Eugenio, F., et al. 2026, MNRAS, 548, staf2109
Mandel, H., Appenzeller, I., Bomans, D., et al. 2000, SPIE Conf. Ser., 4008, 767
Martínez-Ramírez, L. N., Wolf, J., Belladitta, S., et al. 2026, A&A, 708, A117
Matsuoka, Y., Onoue, M., Iwasawa, K., et al. 2023, ApJ, 949, L42
McLean, I. S., Steidel, C. C., Epps, H., et al. 2010, SPIE Conf. Ser., 7735, 77351E
McLean, I. S., Steidel, C. C., Epps, H. W., et al. 2012, SPIE Conf. Ser., 8446, 84460J
Meyer, R. A., Bosman, S. E. I., & Ellis, R. S. 2019, MNRAS, 487, 3305
Milosavljević, M., Couch, S. M., & Bromm, V. 2009, ApJ, 696, L146
Mortlock, D. J., Warren, S. J., Venemans, B. P., et al. 2011, Nature, 474, 616
Naidu, R. P., Matthee, J., Katz, H., et al. 2026, Nature, 656, 329
Nanni, R., Hennawi, J. F., Wang, F., et al. 2022, MNRAS, 515, 3224
Napolitano, L., Castellano, M., Pentericci, L., et al. 2025, ApJ, 989, 75
Natarajan, P. 2011, Bull. Astron. Soc. India, 39, 145
Neeleman, M., Novak, M., Venemans, B. P., et al. 2021, ApJ, 911, 141
Netzer, H. 2013, The Physics and Evolution of Active Galactic Nuclei (Cambridge University Press)
Netzer, H., Shemmer, O., Maiolino, R., et al. 2004, ApJ, 614, 558
Oke, J. B., & Gunn, J. E. 1983, ApJ, 266, 713
Onorato, S., Hennawi, J. F., Schindler, J.-T., et al. 2025, MNRAS, 540, 1308
Onoue, M., Kashikawa, N., Matsuoka, Y., et al. 2019, ApJ, 880, 77
Pacucci, F., & Loeb, A. 2020, ApJ, 895, 95
Pâris, I., Petitjean, P., Aubourg, É., et al. 2018, A&A, 613, A51
Park, D., Barth, A. J., Ho, L. C., & Laor, A. 2022, ApJS, 258, 38
Pedregosa, F., Varoquaux, G., Gramfort, A., et al. 2011, JMLR, 12, 2825
Pizzati, E., Hennawi, J. F., Schaye, J., et al. 2024, MNRAS, 534, 3155
Planck Collaboration VI. 2020, A&A, 641, A6
Poutanen, J., Lipunova, G., Fabrika, S., Butkevich, A. G., & Abolmasov, P. 2007, MNRAS, 377, 1187
Prochaska, J. X. 2017, Astron. Comput., 19, 27
Prochaska, J. X., Hennawi, J. F., & Herbert-Fort, S. 2008, ApJ, 675, 1002
Prochaska, J. X., Hennawi, J., Cooke, R., et al. 2020a, https://doi.org/10.5281/zenodo.3743493
Prochaska, J. X., Hennawi, J. F., Westfall, K. B., et al. 2020b, JOSS, 5, 2308
Rieke, M. J., Kelly, D. M., Misselt, K., et al. 2023, PASP, 135, 028001
Rigby, J., Perrin, M., McElwain, M., et al. 2023, PASP, 135, 048001
Rowlands, S., Davies, R. L., Ryan-Weber, E., et al. 2026, MNRAS, 546, staf2254
Rubin, S. G., Sakharov, A. S., & Khlopov, M. Y. 2001, Sov. Phys. JETP, 92, 921
Runnoe, J. C., Brotherton, M. S., & Shang, Z. 2012a, MNRAS, 427, 1800
Runnoe, J. C., Brotherton, M. S., & Shang, Z. 2012b, MNRAS, 422, 478
Russell, D. M., Ellison, S. L., & Benn, C. R. 2006, MNRAS, 367, 412
Sakurai, Y., Yoshida, N., Fujii, M. S., & Hirano, S. 2017, MNRAS, 472, 1677
Salpeter, E. E. 1964, ApJ, 140, 796
Salviander, S., Shields, G. A., Gebhardt, K., & Bonning, E. W. 2007, ApJ, 662, 131
Schindler, J.-T., Farina, E. P., Bañados, E., et al. 2020, ApJ, 905, 51

Schindler, J.-T., Bañados, E., Connor, T., et al. 2023, ApJ, 943, 67
Schindler, J.-T., Hennawi, J. F., Davies, F. B., et al. 2026, A&A, 708, A160
Schirmer, M. 2026, eummy: A Tool to Create Color Images from Euclid MER Stacks, Python Package Index (PyPI), https://pypi.org/project/eummy/, version 1.3.2
Seifert, W., Appenzeller, I., Baumeister, H., et al. 2003, SPIE Conf. Ser., 4841, 962
Shakura, N. I., & Sunyaev, R. A. 1973, A&A, 24, 337
Shen, Y., Richards, G. T., Strauss, M. A., et al. 2011, ApJS, 194, 45
Shimura, T., & Manmoto, T. 2003, MNRAS, 338, 1013
Sigut, T. A. A., & Pradhan, A. K. 2003, ApJS, 145, 15
Silverman, J. D., Li, J., Ding, X., et al. 2025, ApJ, 995, L67
Smit, R., & Bowler, R. A. A. 2026, ARA&A, 64, 493
Stern, J., & Laor, A. 2012, MNRAS, 426, 2703
Stern, D., Spinrad, H., Eisenhardt, P., et al. 2000, ApJ, 533, L75
Stone, M. A., Lyu, J., Rieke, G. H., & Alberts, S. 2023, ApJ, 953, 180
Stone, M. A., Lyu, J., Rieke, G. H., Alberts, S., & Hainline, K. N. 2024, ApJ, 964, 90
Tanaka, T. S., Akins, H. B., Harikane, Y., et al. 2025, ApJ, 995, 21
Taylor, A. J., Kokorev, V., Kocevski, D. D., et al. 2025, ApJ, 989, L7
Thorne, K. S. 1974, ApJ, 191, 507
Tie, S. S., Hennawi, J. F., Wang, F., et al. 2024, MNRAS, 535, 223
Trinca, A., Lupi, A., Haiman, Z., et al. 2026, MNRAS, 551, stag1230
Vanden Berk, D. E., Richards, G. T., Bauer, A., et al. 2001, AJ, 122, 549
Venemans, B. P., Walter, F., Neeleman, M., et al. 2020, ApJ, 904, 130
Vestergaard, M., & Osmer, P. S. 2009, ApJ, 699, 800
Vestergaard, M., & Peterson, B. M. 2006, ApJ, 641, 689
Vestergaard, M., & Wilkes, B. J. 2001, ApJS, 134, 1
Volonteri, M. 2010, A&ARv, 18, 279
Volonteri, M., Madau, P., Quataert, E., & Rees, M. J. 2005, ApJ, 620, 69
Volonteri, M., Lodato, G., & Natarajan, P. 2008, MNRAS, 383, 1079
Volonteri, M., Pfister, H., Beckmann, R. S., et al. 2020, MNRAS, 498, 2219
Wang, F., Yang, J., Fan, X., et al. 2021, ApJ, 907, L1
Wang, F., Champagne, J. B., Huang, J., et al. 2026, ApJ, 1006, 39
Watson, P. J., Vulcani, B., Treu, T., et al. 2025, A&A, 699, A225
Whalen, D., van Veelen, B., O'Shea, B. W., & Norman, M. L. 2008, ApJ, 682, 49
Willott, C. J., Delorme, P., Omont, A., et al. 2007, AJ, 134, 2435
Wolf, J., Salvato, M., Belladitta, S., et al. 2024, A&A, 691, A30
Wolf, J., Bañados, E., Fan, X., et al. 2026, A&A, 707, A299
Woo, J.-H., Kim, J., Cho, H., & Wang, S. 2026, ApJ, 1003, 123
Wu, Q., & Shen, Y. 2022, ApJS, 263, 42
Yang, J., Wang, F., Fan, X., et al. 2020, ApJ, 897, L14
Yang, J., Wang, F., Fan, X., et al. 2021, ApJ, 923, 262
Yang, J., Fan, X., Gupta, A., et al. 2023, ApJS, 269, 27
Yang, D.-M., Schindler, J.-T., Nanni, R., et al. 2024, MNRAS, 528, 2679
Yang, D., Hennawi, J. F., Guarneri, F., et al. 2026, A&A, 711, A104
Young, P. J., Sargent, W. L. W., Boksenberg, A., Carswell, R. F., & Whelan, J. A. J. 1979, ApJ, 229, 891
Yue, M., Eilers, A.-C., Simcoe, R. A., et al. 2024, ApJ, 966, 176
Zamora, S., Carniani, S., Bertola, E., et al. 2025, A&A, accepted [arXiv:2512.09022]
Ziparo, F., Gallerani, S., & Ferrara, A. 2025, JCAP, 04, 040
Zou, F., Gallo, E., Zuo, Z., et al. 2026, ApJ, accepted [arXiv:2603.24893]

Authors and affiliations

J. Wolf[1,2,3,★★], S. Belladitta[1,4], D. Yang[5], F. Guarneri[6,7], E. Bañados[1], J. F. Hennawi[8,5], J.-T. Schindler[6], R. E. Hviding[1], K. Jahnke[1], D. J. Mortlock[9,10], X. Fan[11], D. Stern[12], A.-C. Eilers[13,14], F. Wang[15], J. Yang[15], S. E. I. Bosman[16,1], C. J. Conselice[17], F. B. Davies[1], R. Decarli[4], A. C. N. Hughes[9], I. G. Momcheva[1], M. Onoue[18,19], L. N. Martinez-Ramirez[6], R. A. A. Bowler[17], M. Castellano[20], P. Dayal[21,22,23], Y. Matsuoka[24], Y. Fu[5,25], H. J. A. Rottgering[5], M. Salvato[26], J. Calhau[27], K. I. Caputi[25], G. Castignani[4], Y. Copin[28], A. de Graaff[1], J. M. Diego[29], P. R. M. Eisenhardt[12], A. Fontana[20], C. M. Gutierrez[30,31], Y. Harikane[32], H. Hoekstra[5], R. Maiolino[33], M. Schirmer[1], D. Scott[34], T. Sekine[6], F. Shankar[35], S. Serjeant[36], L. Spinoglio[37], G. Vietri[38], F. Walter[1], G. Zamorani[4], S. Andreon[39], C. Baccigalupi[40,7,41,42], M. Baldi[43,4,44], P. Battaglia[4], R. Bender[26,45], A. Biviano[7,40], M. Bolzonella[4], E. Branchini[46,47,39], M. Brescia[48,27], J. Brinchmann[49,50,2], S. Camera[51,52,53], G. Cañas-Herrera[5], V. Capobianco[53], C. Carbone[38], J. Carretero[54,55], F. J. Castander[56,57], S. Cavuoti[27,58], K. C. Chambers[59], A. Cimatti[60], C. Colodro-Conde[30], G. Congedo[61], L. Conversi[62,63], F. Courbin[64,65,66], H. M. Courtois[67], M. Cropper[68], J.-G. Cuby[69,70], H. Degaudenzi[71], G. De Lucia[7], H. Dole[72], F. Dubath[71], X. Dupac[63], S. Escoffier[73], M. Fabricius[26,45], M. Farina[37], R. Farinelli[4], S. Ferriol[28], P. Fosalba[57,56], S. Fotopoulou[74], N. Fourmanoit[73], M. Fumana[38], L. Gabarra[75], S. Galeotta[7], K. George[45], B. Gillis[61], C. Giocoli[4,44], J. Gracia-Carpio[26], A. Grazian[76], F. Grupp[26,45], S. V. H. Haugan[77], S. Hemmati[78], W. Holmes[12], I. M. Hook[79], F. Hormuth[80], A. Hornstrup[81,82], M. Huertas-Company[30,83,84], M. Jhabvala[85], B. Joachimi[86], S. Kermiche[73], A. Kiessling[12], B. Kubik[28], K. Kuijken[5], M. Kümmel[45], M. Kunz[87], H. Kurki-Suonio[88,89], R. Laureijs[25], A. M. C. Le Brun[90], V. Le Brun[70], S. Ligori[53], P. B. Lilje[77], I. Lloro[91], M. Maglioccheti[37], G. Mainetti[92], D. Maino[93,38,94], E. Maiorano[4], O. Mansutti[7], O. Marggraf[95], M. Martinelli[20,96], N. Martinet[70], F. Marulli[97,4,44], R. J. Massey[98], D. C. Masters[99], N. Mauri[60,44], C. J. R. McPartland[82,100], E. Medinaceli[4], S. Mei[101,102], M. Meneghetti[4,44], E. Merlin[76], G. Meylan[103], P. Monaco[104,7,41,40], A. Mora[105], M. Moresco[97,4], C. Moretti[7,40,41], L. Moscardini[97,4,44], R. Nakajima[95], C. Neissner[106,55], R. C. Nichol[107], S.-M. Niemi[108], C. Padilla[106], S. Paltani[71], F. Pasian[7], W. J. Percival[109,110,111], V. Pettorino[108], S. Pires[112], G. Polenta[113], M. Poncet[114], L. A. Popa[115], F. Raison[26], R. Rebolo[30,116,31], A. Renzi[117,118,4], J. Rhodes[12], G. Riccio[27], I. Risso[46,47,39], H.-W. Rix[1], F. Rizzo[7], E. Romelli[7], M. Roncarelli[4], R. Saglia[45,26], Z. Sakr[119,120,121], D. Sapone[122], M. Sauvage[112], J. A. Schewtschenko[61], P. Schneider[95], T. Schrabback[123], A. Secroun[73], E. Sihvola[124], P. Simon[95], C. Sirignano[117,118], G. Sirri[44], L. Stanco[118], P. Tallada-Crespí[54,55], A. N. Taylor[61], I. Tereno[125,126], N. Tessore[68], S. Toft[82,100], R. Toledo-Moreo[127,128], F. Torradeflot[55,54], I. Tutusaus[56,57,120], E. A. Valentijn[25], L. Valenziano[4,129], J. Valiviita[88,89], T. Vassallo[7,45], D. Vibert[70], Y. Wang[78], J. Weller[45,26], F. M. Zerbi[39], E. Zucca[4], and J. García-Bellido[119]

[1] Max-Planck-Institut für Astronomie, Königstuhl 17, 69117 Heidelberg, Germany
[2] European Southern Observatory, Karl-Schwarzschild-Str. 2, 85748 Garching, Germany
[3] Excellence Cluster ORIGINS, Boltzmannstrasse 2, 85748 Garching, Germany
[4] INAF-Osservatorio di Astrofisica e Scienza dello Spazio di Bologna, Via Piero Gobetti 93/3, 40129 Bologna, Italy
[5] Leiden Observatory, Leiden University, Einsteinweg 55, 2333 CC Leiden, The Netherlands
[6] Hamburger Sternwarte, University of Hamburg, Gojenbergsweg 112, 21029 Hamburg, Germany
[7] INAF-Osservatorio Astronomico di Trieste, Via G. B. Tiepolo 11, 34143 Trieste, Italy
[8] Department of Physics, University of California, Santa Barbara, CA 93106, USA
[9] Astrophysics Group, Blackett Laboratory, Imperial College London, London SW7 2AZ, UK
[10] Department of Mathematics, Imperial College London, London SW7 2AZ, UK
[11] Steward Observatory, University of Arizona, 933 N. Cherry Ave, Tucson, AZ 85750, USA
[12] Jet Propulsion Laboratory, California Institute of Technology, 4800 Oak Grove Drive, Pasadena, CA 91109, USA
[13] Department of Physics, Massachusetts Institute of Technology, Cambridge, MA 02139, USA
[14] MIT Kavli Institute for Astrophysics and Space Research, Massachusetts Institute of Technology, Cambridge, MA 02139, USA
[15] Department of Astronomy, University of Michigan, 1085 S. University Ave., Ann Arbor, MI 48109, USA
[16] Institut für Theoretische Physik, University of Heidelberg, Philosophenweg 16, 69120 Heidelberg, Germany
[17] Jodrell Bank Centre for Astrophysics, Department of Physics and Astronomy, University of Manchester, Oxford Road, Manchester M13 9PL, UK
[18] Waseda Institute for Advanced Study (WIAS), Waseda University, 1-21-1, Nishi-Waseda, Shinjuku, Tokyo 169-0051, Japan
[19] Kavli Institute for the Physics and Mathematics of the Universe (WPI), University of Tokyo, Kashiwa, Chiba 277-8583, Japan
[20] INAF-Osservatorio Astronomico di Roma, Via Frascati 33, 00078 Monteporzio Catone, Italy
[21] Canadian Institute for Theoretical Astrophysics, Toronto ON M5S 3H8, Canada
[22] David A. Dunlap Department of Astronomy & Astrophysics, University of Toronto, 50 St George Street, Toronto, Ontario M5S 3H4, Canada
[23] Department of Physics, 60 St George St, University of Toronto, Toronto, ON M5S 3H8, Canada

[24] Research Center for Space and Cosmic Evolution, Ehime University, 2-5 Bunkyo-cho, Matsuyama, Ehime 790-8577, Japan
[25] Kapteyn Astronomical Institute, University of Groningen, PO Box 800, 9700 AV Groningen, The Netherlands
[26] Max Planck Institute for Extraterrestrial Physics, Giessenbachstr. 1, 85748 Garching, Germany
[27] INAF-Osservatorio Astronomico di Capodimonte, Via Moiariello 16, 80131 Napoli, Italy
[28] Université Claude Bernard Lyon 1, CNRS/IN2P3, IP2I Lyon, UMR 5822, Villeurbanne F-69100, France
[29] Instituto de Física de Cantabria, Edificio Juan Jordá, Avenida de los Castros, 39005 Santander, Spain
[30] Instituto de Astrofísica de Canarias, E-38205 La Laguna, Tenerife, Spain
[31] Universidad de La Laguna, Dpto. Astrofísica, E-38206 La Laguna, Tenerife, Spain
[32] Institute for Cosmic Ray Research, The University of Tokyo, 5-1-5 Kashiwanoha, Kashiwa, Chiba 277-8582, Japan
[33] Cavendish Laboratory, University of Cambridge, JJ Thomson Avenue, Cambridge CB3 0HE, UK
[34] Department of Physics and Astronomy, University of British Columbia, Vancouver BC V6T 1Z1, Canada
[35] School of Physics & Astronomy, University of Southampton, Highfield Campus, Southampton SO17 1BJ, UK
[36] School of Physical Sciences, The Open University, Milton Keynes MK7 6AA, UK
[37] INAF-Istituto di Astrofisica e Planetologia Spaziali, Via del Fosso del Cavaliere, 100, 00100 Roma, Italy
[38] INAF-IASF Milano, Via Alfonso Corti 12, 20133 Milano, Italy
[39] INAF-Osservatorio Astronomico di Brera, Via Brera 28, 20122 Milano, Italy
[40] IFPU, Institute for Fundamental Physics of the Universe, Via Beirut 2, 34151 Trieste, Italy
[41] INFN, Sezione di Trieste, Via Valerio 2, 34127, Trieste, TS, Italy
[42] SISSA, International School for Advanced Studies, Via Bonomea 265, 34136 Trieste, TS, Italy
[43] Dipartimento di Fisica e Astronomia, Università di Bologna, Via Gobetti 93/2, 40129 Bologna, Italy
[44] INFN-Sezione di Bologna, Viale Berti Pichat 6/2, 40127 Bologna, Italy
[45] Universitäts-Sternwarte München, Fakultät für Physik, Ludwig-Maximilians-Universität München, Scheinerstr. 1, 81679 München, Germany
[46] Dipartimento di Fisica, Università di Genova, Via Dodecaneso 33, 16146 Genova, Italy
[47] INFN-Sezione di Genova, Via Dodecaneso 33, 16146 Genova, Italy
[48] Department of Physics "E. Pancini", University Federico II, Via Cinthia 6, 80126 Napoli, Italy
[49] Instituto de Astrofísica e Ciências do Espaço, Universidade do Porto, CAUP, Rua das Estrelas, PT4150-762 Porto, Portugal
[50] Faculdade de Ciências da Universidade do Porto, Rua do Campo de Alegre, 4150-007 Porto, Portugal
[51] Dipartimento di Fisica, Università degli Studi di Torino, Via P. Giuria 1, 10125 Torino, Italy
[52] INFN-Sezione di Torino, Via P. Giuria 1, 10125 Torino, Italy
[53] INAF-Osservatorio Astrofisico di Torino, Via Osservatorio 20, 10025 Pino Torinese (TO), Italy
[54] Centro de Investigaciones Energéticas, Medioambientales y Tecnológicas (CIEMAT), Avenida Complutense 40, 28040 Madrid, Spain
[55] Port d'Informació Científica, Campus UAB, C. Albareda s/n, 08193 Bellaterra (Barcelona), Spain
[56] Institute of Space Sciences (ICE, CSIC), Campus UAB, Carrer de Can Magrans, s/n, 08193 Barcelona, Spain
[57] Institut d'Estudis Espacials de Catalunya (IEEC), Edifici RDIT, Campus UPC, 08860 Castelldefels, Barcelona, Spain
[58] INFN – Sezione di Napoli, Via Cinthia 6, 80126 Napoli, Italy
[59] Institute for Astronomy, University of Hawaii, 2680 Woodlawn Drive, Honolulu, HI 96822, USA
[60] Dipartimento di Fisica e Astronomia "Augusto Righi" – Alma Mater Studiorum Università di Bologna, Viale Berti Pichat 6/2, 40127 Bologna, Italy
[61] Institute for Astronomy, University of Edinburgh, Royal Observatory, Blackford Hill, Edinburgh EH9 3HJ, UK
[62] European Space Agency/ESRIN, Largo Galileo Galilei 1, 00044 Frascati, Roma, Italy
[63] ESAC/ESA, Camino Bajo del Castillo, s/n., Urb. Villafranca del Castillo, 28692 Villanueva de la Cañada, Madrid, Spain
[64] Institut de Ciències del Cosmos (ICCUB), Universitat de Barcelona (IEEC-UB), Martí i Franquès 1, 08028 Barcelona, Spain
[65] Institució Catalana de Recerca i Estudis Avançats (ICREA), Passeig de Lluís Companys 23, 08010 Barcelona, Spain
[66] Institut de Ciencies de l'Espai (IEEC-CSIC), Campus UAB, Carrer de Can Magrans, s/n Cerdanyola del Vallés, 08193 Barcelona, Spain
[67] UCB Lyon 1, CNRS/IN2P3, IUF, IP2I Lyon, 4 rue Enrico Fermi, 69622 Villeurbanne, France
[68] Mullard Space Science Laboratory, University College London, Holmbury St Mary, Dorking, Surrey RH5 6NT, UK
[69] Canada-France-Hawaii Telescope, 65-1238 Mamalahoa Hwy, Kamuela, HI 96743, USA
[70] Aix-Marseille Université, CNRS, CNES, LAM, Marseille, France
[71] Department of Astronomy, University of Geneva, ch. d'Ecogia 16, 1290 Versoix, Switzerland
[72] Université Paris-Saclay, CNRS, Institut d'astrophysique spatiale, 91405 Orsay, France
[73] Aix-Marseille Université, CNRS/IN2P3, CPPM, Marseille, France
[74] School of Physics, HH Wills Physics Laboratory, University of Bristol, Tyndall Avenue, Bristol BS8 1TL, UK
[75] Department of Physics, University of Oxford, Keble Road, Oxford OX1 3RH, UK
[76] INAF-Osservatorio Astronomico di Padova, Via dell'Osservatorio 5, 35122 Padova, Italy
[77] Institute of Theoretical Astrophysics, University of Oslo, P.O. Box 1029, Blindern 0315, Oslo, Norway
[78] Caltech/IPAC, 1200 E. California Blvd., Pasadena, CA 91125, USA
[79] Department of Physics, Lancaster University, Lancaster LA1 4YB, UK
[80] Felix Hormuth Engineering, Goethestr. 17, 69181 Leimen, Germany
[81] Technical University of Denmark, Elektrovej 327, 2800 Kgs. Lyngby, Denmark
[82] Cosmic Dawn Center (DAWN), Denmark
[83] Université PSL, Observatoire de Paris, Sorbonne Université, CNRS, LERMA, 75014 Paris, France
[84] Université Paris-Cité, 5 Rue Thomas Mann, 75013 Paris, France
[85] NASA Goddard Space Flight Center, Greenbelt, MD 20771, USA
[86] Department of Physics and Astronomy, University College London, Gower Street, London WC1E 6BT, UK
[87] Université de Genève, Département de Physique Théorique and Centre for Astroparticle Physics, 24 quai Ernest-Ansermet, CH-1211 Genève 4, Switzerland
[88] Department of Physics, P.O. Box 64, University of Helsinki, 00014 Helsinki, Finland
[89] Helsinki Institute of Physics, Gustaf Hällströmin katu 2, University of Helsinki, 00014 Helsinki, Finland

[90] Laboratoire d'etude de l'Univers et des phenomenes eXtremes, Observatoire de Paris, Université PSL, Sorbonne Université, CNRS, 92190 Meudon, France
[91] SKAO, Jodrell Bank, Lower Withington, Macclesfield SK11 9FT, UK
[92] Centre de Calcul de l'IN2P3/CNRS, 21 avenue Pierre de Coubertin, 69627 Villeurbanne Cedex, France
[93] Dipartimento di Fisica "Aldo Pontremoli", Università degli Studi di Milano, Via Celoria 16, 20133 Milano, Italy
[94] INFN-Sezione di Milano, Via Celoria 16, 20133 Milano, Italy
[95] Universität Bonn, Argelander-Institut für Astronomie, Auf dem Hügel 71, 53121 Bonn, Germany
[96] INFN-Sezione di Roma, Piazzale Aldo Moro, 2 – c/o Dipartimento di Fisica, Edificio G. Marconi, 00185 Roma, Italy
[97] Dipartimento di Fisica e Astronomia "Augusto Righi" – Alma Mater Studiorum Università di Bologna, Via Piero Gobetti 93/2, 40129 Bologna, Italy
[98] Department of Physics, Institute for Computational Cosmology, Durham University, South Road, Durham DH1 3LE, UK
[99] Infrared Processing and Analysis Center, California Institute of Technology, Pasadena, CA 91125, USA
[100] Niels Bohr Institute, University of Copenhagen, Jagtvej 128, 2200 Copenhagen, Denmark
[101] Université Paris Cité, CNRS, Astroparticule et Cosmologie, 75013 Paris, France
[102] CNRS-UCB International Research Laboratory, Centre Pierre Binétruy, IRL2007, CPB-IN2P3 Berkeley, USA
[103] Institute of Physics, Laboratory of Astrophysics, Ecole Polytechnique Fédérale de Lausanne (EPFL), Observatoire de Sauverny, 1290 Versoix, Switzerland
[104] Dipartimento di Fisica – Sezione di Astronomia, Università di Trieste, Via Tiepolo 11, 34131 Trieste, Italy
[105] Telespazio UK S.L. for European Space Agency (ESA), Camino bajo del Castillo, s/n, Urbanizacion Villafranca del Castillo, Villanueva de la Cañada 28692 Madrid, Spain
[106] Institut de Física d'Altes Energies (IFAE), The Barcelona Institute of Science and Technology, Campus UAB, 08193 Bellaterra (Barcelona), Spain
[107] School of Mathematics and Physics, University of Surrey, Guildford, Surrey GU2 7XH, UK
[108] European Space Agency/ESTEC, Keplerlaan 1, 2201 AZ Noordwijk, The Netherlands
[109] Waterloo Centre for Astrophysics, University of Waterloo, Waterloo, Ontario N2L 3G1, Canada
[110] Department of Physics and Astronomy, University of Waterloo, Waterloo, Ontario N2L 3G1, Canada
[111] Perimeter Institute for Theoretical Physics, Waterloo, Ontario N2L 2Y5, Canada
[112] Université Paris-Saclay, Université Paris Cité, CEA, CNRS, AIM, 91191 Gif-sur-Yvette, France
[113] Space Science Data Center, Italian Space Agency, Via del Politecnico snc, 00133 Roma, Italy
[114] Centre National d'Etudes Spatiales – Centre spatial de Toulouse, 18 avenue Edouard Belin, 31401 Toulouse Cedex 9, France
[115] Institute of Space Science, Str. Atomistilor, nr. 409 Măgurele, Ilfov 077125, Romania
[116] Consejo Superior de Investigaciones Cientificas, Calle Serrano 117, 28006 Madrid, Spain
[117] Dipartimento di Fisica e Astronomia "G. Galilei", Università di Padova, Via Marzolo 8, 35131 Padova, Italy
[118] INFN-Padova, Via Marzolo 8, 35131 Padova, Italy
[119] Instituto de Física Teórica UAM-CSIC, Campus de Cantoblanco, 28049 Madrid, Spain
[120] Institut de Recherche en Astrophysique et Planétologie (IRAP), Université de Toulouse, CNRS, UPS, CNES, 14 Av. Edouard Belin, 31400 Toulouse, France
[121] Université St Joseph; Faculty of Sciences, Beirut, Lebanon
[122] Departamento de Física, FCFM, Universidad de Chile, Blanco Encalada 2008, Santiago, Chile
[123] Universität Innsbruck, Institut für Astro- und Teilchenphysik, Technikerstr. 25/8, 6020 Innsbruck, Austria
[124] Department of Physics and Helsinki Institute of Physics, Gustaf Hällströmin katu 2, University of Helsinki, 00014 Helsinki, Finland
[125] Departamento de Física, Faculdade de Ciências, Universidade de Lisboa, Edifício C8, Campo Grande, PT1749-016 Lisboa, Portugal
[126] Instituto de Astrofísica e Ciências do Espaço, Faculdade de Ciências, Universidade de Lisboa, Tapada da Ajuda, 1349-018 Lisboa, Portugal
[127] Universidad Politécnica de Cartagena, Departamento de Electrónica y Tecnología de Computadoras, Plaza del Hospital 1, 30202 Cartagena, Spain
[128] European University of Technology, European Union
[129] INFN-Bologna, Via Irnerio 46, 40126 Bologna, Italy

** Corresponding author: julien.wolf@eso.org

Appendix A: Lower redshift SDSS quasar analogues

We search for the most similar quasars to J1504+6252 within the data release 14 Quasar catalogue (DR14Q) from the extended Baryon Oscillation Spectroscopic Survey (eBOSS) of the Sloan Digital Sky Survey IV (SDSS-IV, Pâris et al. 2018), which we access via `igmspec` (Prochaska 2017). The nearest-neighbour search and the parent sample are the same as described in Bosman et al. (2021). In order to cover the spectrum from the Ly α up to the C III] λ1909 emission line, we select quasars with $2.7 < z < 3.5$ with spectral S/N > 7 and no presence of broad absorption lines; this yields 9194 low-z quasars. The continua are compared over 123 nm $< \lambda_{\rm rest} <$ 200 nm in order to avoid the Lyman-α absorption damping wing in J1504+6252. The spectra are automatically fit with a spline following the procedure outlined by Young et al. (1979) and Carswell et al. (1982), first implemented by Dall'Aglio et al. (2008) and with the improvements of Davies et al. (2018b) and Bosman et al. (2021). Starting from an initial estimated spline spacing which is equal in velocity space for both J1504+6252 and the low-z sample, the procedure iteratively rejects poor pixels, masks regions affected by absorption, and optimises the placement of spline nodes. Finally, the distances between optimal spline fits were computed using the `NearestNeighbours` module of `sklearn` (Pedregosa et al. 2011) in Euclidean distance. The top 5 nearest neighbours of J1504+6252 within eBOSS have Euclidean distances $d < 3$, which is also typical of the low-z quasar population. The identified analogues are SDSS J1128+3622 (plate–MJD–fibre 4618–55600–0120), SDSS J1140+2813 (6402–56334–0153), SDSS J1542+0818 (5211–56002–0194), SDSS J1457+0519 (4777–55707–0632), and SDSS J1345+2343 (6001–56072–0618). These five best nearest neighbours are shown in Fig. A.1. We note that since the nearest neighbour search stops at $\lambda_{\rm rest} = 2000$ Å, the spectrum is not shown past this value. In the spectral-property catalogue of Wu & Shen (2022), these quasars span redshifts of $z = 2.75$–3.18 and single-epoch C IV-based black-hole masses of $\log_{10}(M_{\rm BH}/M_\odot) = 9.41$–$9.82$. Applying the bolometric corrections adopted by Wu & Shen (2022) to the rest-frame UV continuum luminosities yields bolometric luminosities of $\log_{10}[L_{\rm bol}/({\rm erg\,s^{-1}})] = 46.71$–$47.53$, corresponding to a range of Eddington rates $\lambda_{\rm Edd} = 0.12 - 0.47$. These analogues are thus more luminous than J1504+6252, but their nominal Eddington rates are comparable.

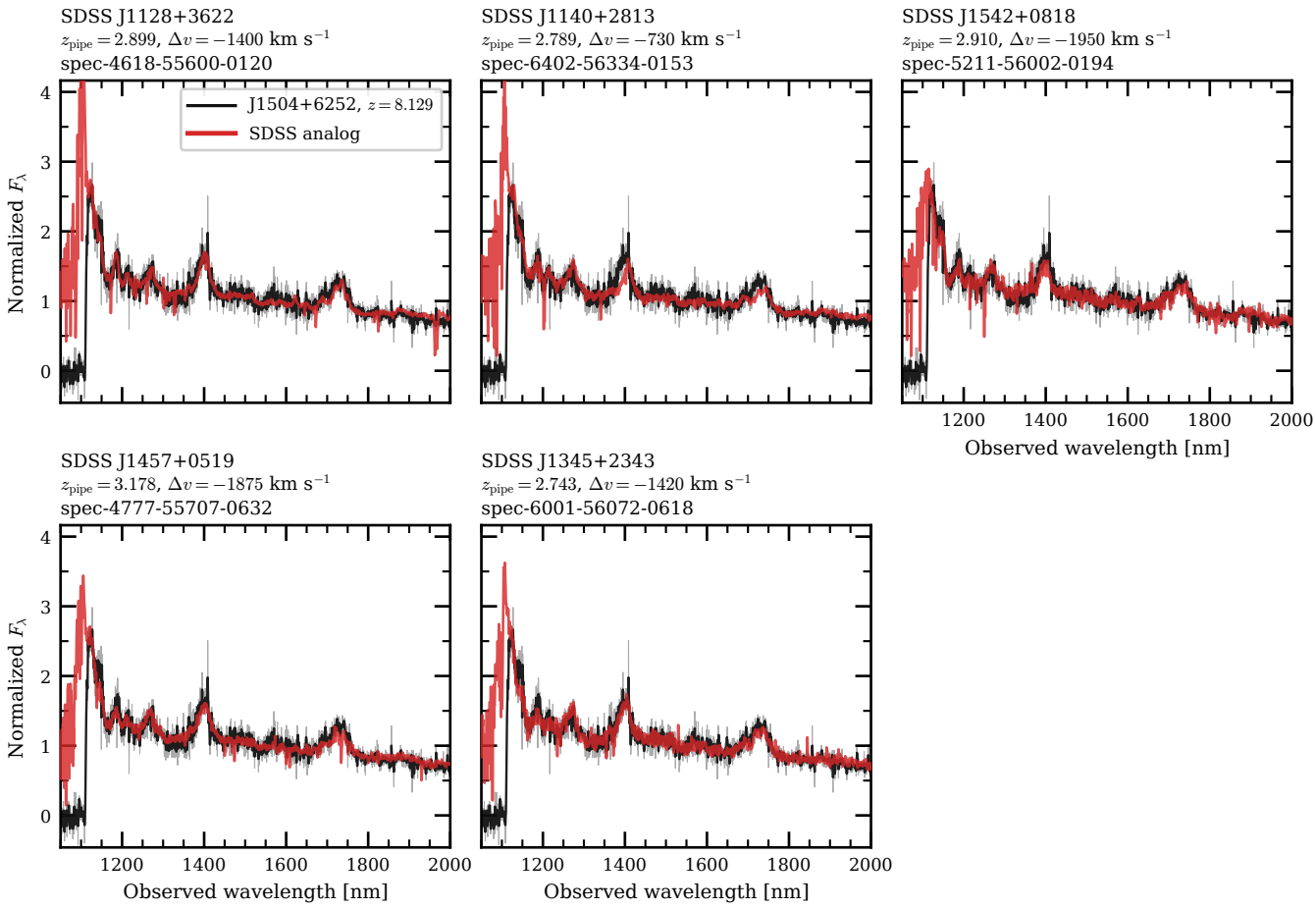


Fig. A.1. Comparison of the rest-frame UV spectrum of J1504+6252 (black) with five lower-redshift SDSS quasars (red) selected as its nearest spectral neighbours. Candidate analogues were identified by minimising the Euclidean distance between continuum-normalised spectra over the common rest-frame wavelength interval 1230–2000 Å. For each comparison quasar, a small velocity offset was additionally fitted to account for intrinsic broad-line centroid shifts before scaling the continuum. The displayed spectra are normalised over the wavelength range 1700–1800 Å. Despite the difference in cosmic age, the overall UV spectral properties of J1504+6252 are remarkably similar to those of several quasars at lower redshift, including the broad emission-line profiles and continuum shape.

Appendix B: Line measurements

In Table B.1, we detail the decomposition of the emission lines used for the estimation of black hole masses in this work.

Table B.1. Emission-line measurements for J1504+6252. Uncertainties correspond to the 16th and 84th percentiles of the posterior distributions. The [O III] values are one-sided posterior 3σ upper limits.

Feature	Component	FWHM [km s^{-1}]	Δv [km s^{-1}]	Flux [10^{-17} erg s^{-1} cm^{-2}]	EW$_0$ [Å]	Comment
Hβ–[O III] complex						
Hβ	Narrow	427^{+153}_{-114}	0	$0.316^{+0.080}_{-0.071}$	$5.90^{+1.51}_{-1.30}$	
Hβ	Intermediate	2294^{+140}_{-216}	-261^{+90}_{-90}	$1.344^{+0.171}_{-0.176}$	$25.12^{+3.30}_{-3.36}$	
Hβ	Broad base	7801^{+532}_{-556}	$+744^{+110}_{-179}$	$2.750^{+0.216}_{-0.212}$	$51.41^{+4.29}_{-4.13}$	
Hβ	BLR total	3159^{+269}_{-272}	$+397^{+92}_{-92}$	$4.096^{+0.192}_{-0.212}$	$76.58^{+4.13}_{-4.68}$	Broad and intermediate components
Hβ	All components	···	$+370^{+82}_{-87}$	$4.413^{+0.189}_{-0.189}$	$82.44^{+4.30}_{-4.17}$	BLR and narrow components
Optical Fe II	4434–4684 Å	1267^{+194}_{-146}	0 (fixed)	$3.134^{+0.212}_{-0.213}$	$51.55^{+4.01}_{-4.08}$	Additional convolution; $R_{\rm FeII} = 0.766^{+0.055}_{-0.050}$
[O III] λ4959	Narrow	427^{+153}_{-114}	0 (tied)	< 0.0237	< 0.463	3σ upper limit
[O III] λ5007	Narrow	427^{+153}_{-114}	0 (tied)	< 0.0706	< 1.407	3σ upper limit
[O III] doublet	Total	427^{+153}_{-114}	0 (tied)	< 0.0943	< 1.870	3σ upper limit
Mg II region						
Mg II	Broad component	3623^{+162}_{-173}	-733^{+58}_{-57}	$2.158^{+0.081}_{-0.083}$	$14.72^{+0.68}_{-0.66}$	Single-component fit
Mg II	BLR doublet profile	3739^{+157}_{-170}	-733^{+58}_{-57}	$2.158^{+0.081}_{-0.083}$	$14.72^{+0.68}_{-0.66}$	FWHM used for $M_{\rm BH}$
UV Fe II	2520–3178 Å	1550^{+265}_{-198}	0 (fixed)	$13.690^{+1.049}_{-0.845}$	$93.39^{+8.53}_{-6.60}$	Final effective FWHM; integrated over the fitted window

Notes. The emission-line FWHM values are intrinsic and account for the instrumental line-spread function. Velocity shifts are measured relative to the adopted systemic reference, with positive values indicating redshifts. The total Hβ BLR profile is the sum of the intermediate and broad-base components, excluding the narrow core. The optical Fe II FWHM is the additional Gaussian convolution applied to the native empirical template and should not be interpreted as the intrinsic Fe II line width. The UV Fe II FWHM is the final effective template width, accounting for the adopted native template FWHM of 900 kms^{-1}. The [O III] widths and velocity shifts are tied to the narrow Hβ component, with $F_{5007}/F_{4959} = 2.98$. The quoted line-flux and equivalent-width uncertainties are derived from the spectral-fit posterior and do not include the 5% absolute-flux-calibration systematic, which is included in the luminosity measurements.